# FORMING HYDRODYNAMICS

**Project F005**

**Report 1**

**to the**

**MEMBER COMPANIES OF THE INSTITUTE OF PAPER SCIENCE AND TECHNOLOGY**

**January 2000**

INSTITUTE OF PAPER SCIENCE AND TECHNOLOGY

Atlanta, Georgia

# FORMING HYDRODYNAMICS

Project F005

Report 1

A Progress Report

to the

MEMBER COMPANIES OF THE INSTITUTE OF PAPER SCIENCE AND TECHNOLOGY

By

C.K. Aidun, V.K.S. Bandhakavi, and J.S. Hooda

January 2000

*An average person in the United States consumes approximately 675 pounds of paper per year as against a world average of about 100 pounds.*

# Contents

# List of Tables

# 1 Paper – an Indispensable Commodity

## 1.1 Introduction

Very few products play as dominant a role as paper does in the lives of human beings. Various paper products that are used in our daily activities include newsprint, coated groundwood (for advertising flyers), business and typing papers for recording, storing, and disseminating information, cardboard boxes for packaging, wrapping paper, towels, and tissues, just to name a few. It is an undeniable fact that the per capita consumption of paper of any country can be used as an index of development like other indices such as consumption of electricity and gas.

Since 105 A.D. when the Chinese invented paper, the paper industry has passed through various phases of development. The 20th century has seen the rapid refinement and modification of the earlier crude technologies, along with the development of such multistage techniques as cooking and bleaching of pulp, papermaking with synthetic fibers, paper drying, paper coating, and computerized process controls, etc. Today the pulp and paper industry provides employment for millions of people all around the world, and especially in the United States and Canada, where it plays a vital role in the overall economy. Also, the rapid increase in automation of various processes in this industry require large investments, which in some cases can reach 1 million dollars per worker and, hence, qualifies the pulp and paper industry as a "capital-intensive industry" [1].

## 1.2 Need for Rapid Advances in Pulp and Paper Industry

The factors that were responsible for North American countries leading the world in the pulp and paper industry are abundant timber, energy, water resources, modern technologies, skilled labor supply, and accessibility to markets. Fortunately, this resulted in a situation where there is no major competition from foreign sources in the domestic market. Continuing globalization of the pulp and paper industry is resulting in the growth of this industry elsewhere in the world. Areas such as Africa, Brazil, and Asia may become large producers of pulp in the coming years. Also, as a result of economic growth in the developing coun-

tries, the utilization of paper is steadily increasing. Some of the requirements placed on the American paper mills by this increased demand and global competition are faster machine speeds, greater product uniformity, and increased production rates. These factors continue to drive the development of new technologies in various spheres of the paper industry such as wet-end operations, pressing/drying technologies, multiple coating trends, to name a few [2].

One of the most significant areas of the current research in the papermaking process is the improvement of wet-end processes, which include the headbox and forming zone. The headbox is the first piece of equipment on a paper machine and a proper design of the same is of vital significance to ensure the quality of the end product. The purpose of headbox is to discharge a rectangular, free surface jet of water with uniformly dispersed wood fibers and fillers. This jet is directed onto the forming table where a fiber mat is formed. Providing a proper turbulence level in the jet, ensuring a uniform distribution of the stock across the machine, with no net cross flow, enhancing fiber dispersion, and suppressing the fiber flocculation at the jet exit are some of the fundamental functions of the headbox. A thorough understanding of the complex hydrodynamics of the headbox, wet-end dynamics such as turbulence, flocculation, stock jet velocity, and impingement angle goes a long way in bridging the gap between the expected quality of the finished paper and the limitations of the existing technologies.

During the last decade, the Fluid Dynamics Group at IPST has investigated these problems from various perspectives. This article presents the efforts and the progress of the more recent work in understanding the headbox hydrodynamics. A number of investigations (both experimental and computational) carried out during the last few years are incorporated in this review report.

In this report we start with the key issues in the paper forming process, with an emphasis on headbox with large-scale and small-scale variations (§2), followed by a detailed analysis of streaks on the forming wire (§3). In §4 we present a Fourier analysis of the surface waves on a forming table and a correlation between the dominating Fourier modes and the length-scale of wet streaks. Effects of two types of secondary flow are discussed in §5 using a numerical

model of the headbox. In §6 we describe the technique of High-Speed Digital Imaging of Paper Forming, which combines high- speed digital imaging, computational image analysis and spectral analysis. This technique is later used for quantitative evaluation of the forming jets from four commercial headboxes which is presented in §7. This is followed by the velocity measurements and analysis of forming jets from laboratory scale headboxes with and without the guide sheets (§8). Conclusions and caveats comprise §9.

# 2 Key Issues in Paper Forming Process

## 2.1 Headbox Requirements

Proper design and operation of the headbox is absolutely critical for an efficient performance of the papermaking process. Readers are referred to a number of books and articles [1,3-5] for a fundamental description of headboxes and various terminology involved in this technology, such as forming table, forming wire, wet streaks, dry line, etc. Here we briefly mention the functions of a modern headbox. The primary function of an ideal headbox is to take the stock (a mixture of pulp and water), delivered by a pipeline, via a fan pump, and transform it into a uniform, rectangular turbulent flow. The width of the jet is the same as that of the paper forming table and the jet has uniform velocity profiles in the machine direction (MD), cross direction (CD), and in the direction normal to the forming table (ZD). While spreading, the jet should evenly disperse the stock across the length, width, and breadth of the forming table. From a practical point of view, this could only be achieved if the jet's velocity profiles have no gradients in MD, CD, and ZD; but do have a controlled level of turbulence to eliminate the fiber flocculation at a scale essential for producing the different grades of paper.

The significance of the headbox in product uniformity is discussed in the next section.

## 2.2 Product Uniformity

Uniformity of physical properties of paper manufactured for printing, packaging, and various other applications is the most serious quality issue in today's mills. Three fundamental physical characteristics of paper are the **density**, the **basis weight** or the weight per unit in-plane area of the sheet, and the **fiber orientation**. These characteristics are of immediate importance since many other physical properties are directly influenced by them to varying degrees. Thus, any variations in basis weight, density, and fiber orientation decide the quality of the finished paper. So, the greater product uniformity coupled with today's faster machine speeds and increased production rates place an enormous demand/responsibility on the papermaking operation. But the quality of sheet formation does not begin at the

forming table, instead, it starts at the headbox. The fundamental characteristics mentioned above depend on various aspects of hydrodynamics of the flow inside the headbox, viz., the secondary flow structure, the homogeneity and uniformity of turbulence at the slice, growth of instabilities after the jet impingement, and the evolution of layer along the forming section. In other words, if the flow from the headbox is not at its best, if the stock is not uniformly distributed across the width of the forming table, if the impingement angle is not properly oriented, if there are too much turbulence, if there are too many velocity gradients (in CD, MD, and ZD), or if there is consistency variation in CD, then too much of the forming table needs to be used to even out the fiber distribution rather than for water draining. This will eventually result in a loss of production rate and/or product quality. In view of the importance of the headbox in the paper formation process, a number of articles have appeared in recent times documenting the challenges facing the papermaking technologies [4,6-8]. Also, in recent years, fine-scale velocity measurements using the High Speed Digital Video Analyzer [9-11] and the Laser Doppler Velocimetry (LDV) [12] (see Appendix A), in conjunction with controlled numerical simulations of headbox flows [10,13-16], have considerably improved our understanding of the complex hydrodynamical processes inside the headbox and at the wet end.

In the next section, we discuss the different scales of nonuniformities.

## 2.3 Large Scale vs. Small Scale Nonuniformities

There are several length scales associated with the physical characteristics of commercially manufactured paper and board. The largest length scale in CD, obviously, is the width of the paper machine. Most paper manufactured today have variations in physical properties of the order of this length scale, such as the variation of average fiber angle in CD. For most of the present-day machines this corresponds to a span greater than 6 in. in CD. These variations are the so-called large scale variations and may result due to the following reasons:

- Overall imbalance in the pressure manifold
- Edge effects in the headbox

- Cross flows due to slice profiling
- Secondary turbulent structures [13]
- Misalignment of a section of the liquid jet with the forming wire
- Misalignment of rolls
- Nonuniform tension and edge effects in the press and dryer sections

Various remedies to correct these large-scale variations are available for implementation. However, some high resolution measurements show that today's commercially manufactured paper and board, have small-scale basis weight variations ranging from 5 to 20%, with peak-to-peak CD spans of $0.5 - 4$ in. For example, basis weight measurements and ultrasonic stiffness measurements by Hall [17] show variations of the order of this length scale. It is not clear at this time if the basis weight variation or the drying rate nonuniformity is the primary cause of the nonuniform elastic stiffness properties. However, the length scale of the fluctuations in physical characteristics is the same as the width of the wet streaks on the forming table. In his experiments, Hall collected extensive measurements of fluid velocities in CD, MD, and ZD on linerboard samples, using ultrasound techniques. The measurements were repeated several times to confirm the existence of small-scale fluctuations. The results from similar measurements overlap, showing real variations in the length scale mentioned above. This reproducibility also shows that with sufficient care, the small-scale variations can be reliably measured and characterized for linerboard and other grades. Since the performance and strength of the product usually depend on the magnitude of the variation in physical properties, the small-scale fluctuations could be more important than the overall averaged nonuniformities. As a result, in this report, we focus our attention mostly on this scale of nonuniformities.

In the subsequent sections, we present a discussion of various investigations (numerical, experimental, and analytical) of the hydrodynamics of headbox and the forming table, mainly carried out by our group at IPST. References to research carried out elsewhere appear where necessary.

# 3 Hydrodynamics of Streaks on the Forming Table

## 3.1 Moisture Streaks and their Causes

Variations in basis weight, which at smaller scale correlate with the distribution of moisture streaks, could have many causes. We categorize these into three classes: (1) nonuniformity in fiber concentration or consistency, (2) nonuniformity in mass distribution on the forming wire or forming table, and (3) nonuniform drainage in the forming section. Of these, we are concerned with the second and third mechanisms, that is, the dynamics of the formation process. The possible nonuniformities caused by the structural defects in the headbox and the forming section are another issue which will not be discussed here.

The smaller scale variations in basis weight, which we consider here, are not well understood and are, therefore, more difficult to eliminate. The magnitudes of the small-scale fluctuations in basis weight are often considerably larger than the magnitude of the basis weight variations recorded by the on-line sensors. Since the performance and strength of the product usually depend on the magnitude of the variation in physical properties, the small-scale fluctuations could be more important than the overall averaged nonuniformities. The small scale fluctuations in elastic stiffness can be caused either by variations in the local sheet density, small-scale variations in fiber orientation, or by the nonuniform drying rate due to moisture streaks in the sheet.

In the next subsection we analyze the streaks on the forming wire.

## 3.2 Variations of Streaks on the Forming Wire

Turbulent flow, by definition, is a combination of high frequency indeterministic random flow fluctuations superimposed on a deterministic mean flow. The time-frozen snap shot of the velocity profile in a turbulent flow shows many fluctuations with an average trend. If a large number of the instantaneous turbulent profiles are added and averaged together, then a smooth profile, referred to as the mean turbulent profile, emerges. In contrast to the random turbulent fluctuations, the mean turbulent profile is a deterministic or predictable quantity.

In order to understand the flow in the forming section over a scale larger than 1/2 inch, we need to focus on the mean turbulent flow on the forming wire. The turbulent fluctuations in the flow are also very important in terms of formation and effects on the evolution of streaks.

Detailed high-speed digital imaging of the forming table is one of the methods that we use in our program to study the physics of paper forming. An elaborate discussion of this technique is presented in a later section (§6). The high-speed images can be taken up to 4000 frames per second with an exposure time as short as 1 microsecond. The small exposure time of a single frame captures the forming layer in a time-frozen form showing the details of the small-scale fluctuations due to turbulent flow. An example of this approach will be presented here with analysis of various regions of the forming section, as outlined in **Fig. 1**.

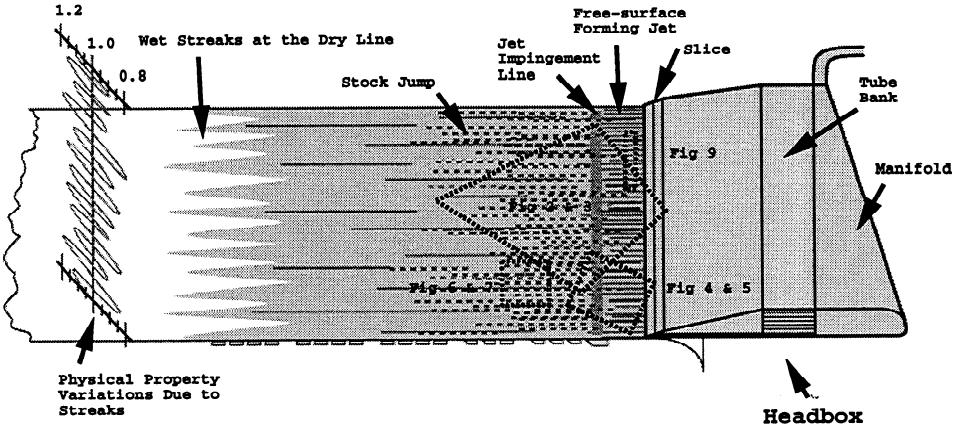


Figure 1: Streaks on the forming table. Locations of the images presented in Figs. 2–8 are outlined.

A single frame of the flow over a large section of the forming table is shown in **Fig. 2**. The machine speed is at 3000 fpm making base sheet for a coated grade. In this view, the slice and the impingement line are covered by the headbox, as indicated in the figure. This image shows many small-scale fluctuations on the forming table. A time-frozen image, as indicated below, is a superposition of randomly occurring flow fluctuations on the mean flow. However, from this image, it is not clear whether there are consistent regularly patterned

streaks on the forming table. To examine this, we need to remove the random fluctuations and look at the mean flow.

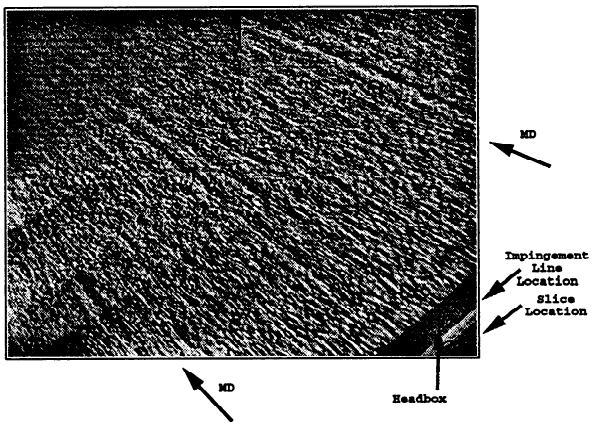


Figure 2: Time-frozen image of the flow over the forming table. (Machine speed = 3000ft/min. Exposure time of the image = $50\mu S$)

By averaging these images over several hundred frames, we can remove the small and randomly occurring features from the image and examine the mean flow. Since the images that we obtain are in digital form, we have developed methods to greatly enhance the image and to take the average of a specified number of images [11]. For this machine speed, an exposure time of 50 microseconds is found to be sufficient. The average flow over 500 frames, each with an exposure time of 50 microseconds taken at a rate of 1000 frames per second covering 0.5 sec in real time, is shown in **Fig. 3**. This image clearly shows that there is a consistent streak pattern in the mean flow over the forming table. To determine the length scale of the streaks, a grid line with tick marks is superimposed on the image. Each division represents 12 inches.

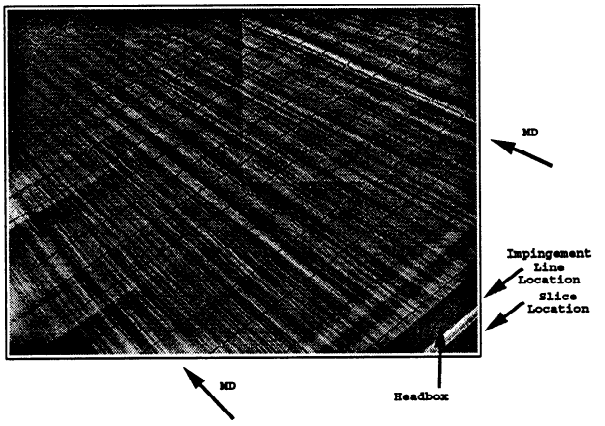


Figure 3: Average of 500 images of the forming table in Fig. 1, covering a period of 0.5 sec. The lines show a 12-inch-long scale in MD and CD.

### 3.3 Amplification of Free Surface Waves at the Impingement Site

As the forming jet delivered from the slice impinges on the wire, the variations in the free surface height, or in other words, the free surface waves or disturbances, amplify due to the forcing of the jet flow along a curved surface. This results in local centrifugal acceleration of the fluid particles normal to the curved surface. At this surface, the local acceleration forces the jet to lose a part of its average kinetic energy to the random fluctuations (the physics is similar to the Rayleigh-Taylor instability [18-21]). The amplification of the disturbances increases with the magnitude of the acceleration or the jet angle: the larger the impingement angle, the greater will be the magnitude of the acceleration. This is due to an acceleration-induced instability which is well understood. The top view of a typical stock jump is shown in **Fig. 4** where the machine direction is from right to left of the figure. This is a single frame taken directly from the top of the wire immediately after the impingement line.

The question is whether one can eliminate the streaks (see **Fig. 3**) on the forming table by strong disturbance of the forming jet and creation of large stock activities at the impingement region. By averaging the top view images of the stock activity after the impingement line, as shown in **Fig. 5**, we examine the character of the flow in this region.

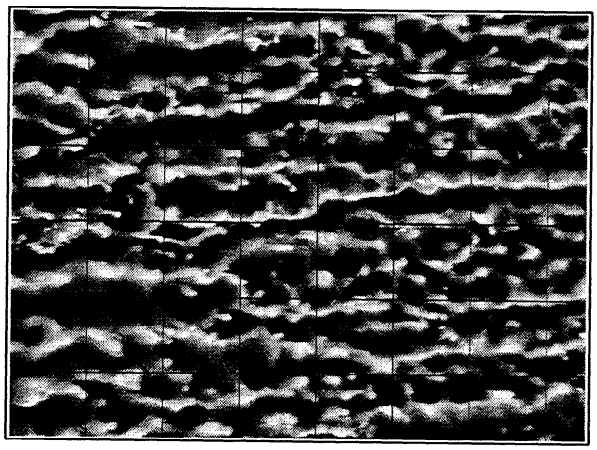

Figure 4: Time-frozen top view image of the stock jump after the impingement line. The MD is from right to left.(Machine speed=3000ft/min, exposure time of the image=$50\mu S$)

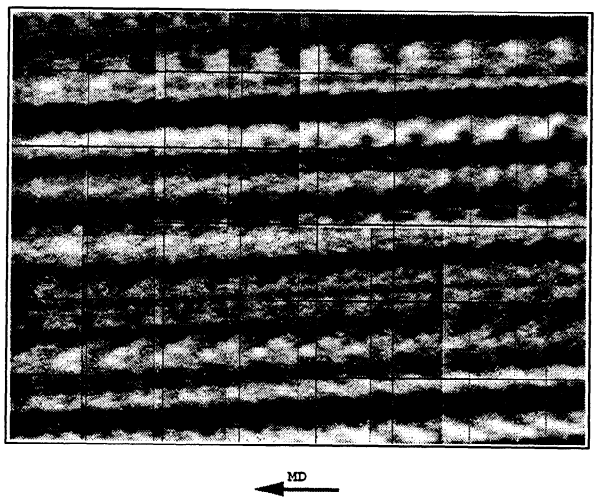


Figure 5: Average of 100 images of the top view image of the stock jump after the impingement line shown in Fig. 4, covering a period of 0.1 sec. The lines show a 1-inch grid line. The MD is from right to left.

It is clear from this figure that the mean free-surface flow of the forming layer at the post-impingement line is nonuniform. A regular streak pattern develops in the mean flow even with severe stock jump. This clearly demonstrates that at least in the situations examined in this study, the regular stock activity on the wire cannot eliminate the streaks in the

forming jet.

In the next subsection we discuss the origin of these streaks.

### 3.4 Origin and Nonuniformities of Streaks

Let us take a closer look at the forming jet delivered from the slice. The enhanced time-frozen image of the forming jet and the impingement line is shown in **Fig. 6**. This image clearly shows streaks in the forming jet that amplify upon impingement on the forming wire and result in some degree of stock jump. Some believe that the streaks in the forming jet are due to the turbulent fluctuations inside the headbox and, therefore, occur randomly in the system. To examine this point, we again take an average of the flow over 0.5 sec. The averaged image is presented in **Fig. 7**. It is clear from the averaged result that the streaks appear consistently, not randomly, in the forming jet. Turbulent fluctuations, however, appear randomly. Therefore, the streaks in the forming jet are not the result of turbulent fluctuations.

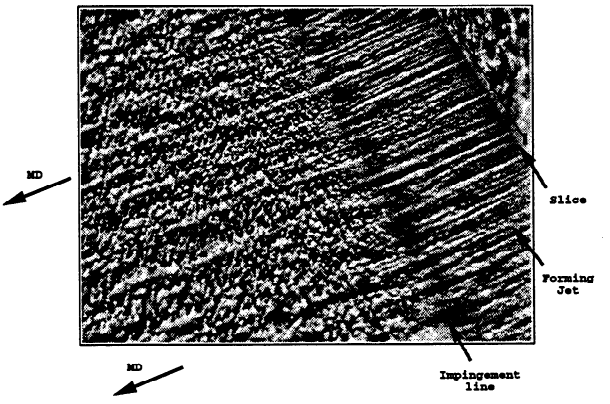


Figure 6: Time-frozen image of the forming jet, jet impingement region, and the stock activity after the impingement line. The marks on the line at slice show a 1-inch-long scale (Machine speed=3000ft/min, exposure time=50$\mu S$.)

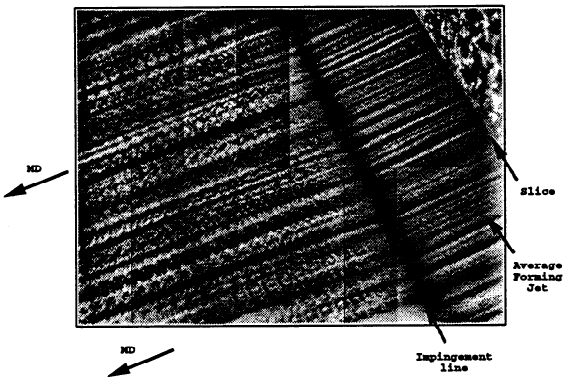


Figure 7: Average of 500 images of the forming region shown in Fig. 4, covering a period of 0.5 sec.

Using large-scale computational methods, we show (1996 IPST report to member companies) that different forms of small-scale secondary flows result from the interaction of the jets from the tubes in the tube bank. The nature of the secondary flows depends on the geometry and size of the tubes and their arrangement pattern in the tube bank.

Now, consider the jets that are delivered by these tubes. The streaks in the forming jet, such as those in **Fig. 7**, are caused by the secondary flows induced by the jets from the tubes. These secondary flows are spatially periodic in nature. That is, there is a given CD span over which the structure of the flow pattern repeats. Let us refer to the CD dimension of this periodic pattern as the width or the wavelength of the secondary flow. The wavelength of the tube jet-induced secondary flow is not necessarily equal to the CD spacing of the tubes in the tube bank. The secondary flows often appear in the form of vortex tubes and recirculating vortices, which are superimposed on the main stream flow. Secondary flows, not to be confused with turbulent fluctuations, are a deterministic part of the flow generated by various mechanisms and can be computed using the mean form of the momentum equation and appropriate turbulent models [13].

In the converging section of the headbox, the vortex tubes stretch along the direction of the flow and cause pressure fluctuations, as shown in **Fig. 8** [22]. The pressure fluctuations, in turn, deform the free surface of the liquid into the streamwise streaks (SS) that we see in **Fig. 6**. The upward and downward streams in the secondary flow form the crest and the

trough of SS, respectively. The structure of SS that form at the slice depends directly on these secondary flows in combination with the nature of the headbox converging zone (i.e., the outlet of the tubes in the tube bank) and the slice geometry. In some cases, there are two SS generated for each column of tubes. Every pair of SS corresponds to a column of tubes. Other types are when SS form from jets delivered by staggered tubes where a weak secondary SS exists next to a stronger primary SS.

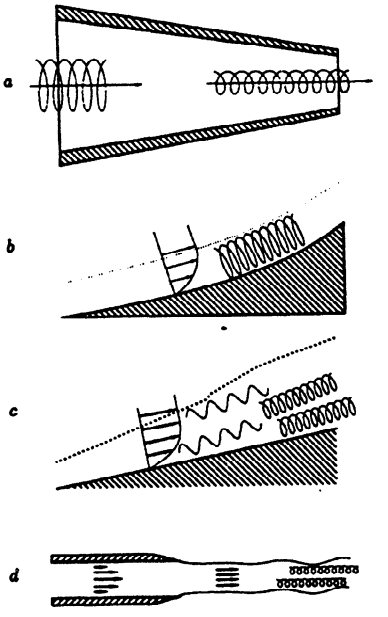


Figure 8: Different types of streak creation, a) Vortex stretching, b) Centrifugal instability, c) boundary layer transition, and d) Wave instability.

Our computational analysis of the interaction between the tube jets inside the headbox reveals the precise form of these secondary flows. Here we have discussed the origin of SS in the forming section. In the next subsection, we discuss the dynamics of SS.

### 3.5 Dynamics of the Streamwise Streaks in the Forming Jet

SS on the forming table are caused by nonuniform or secondary flows in the headbox, the jet interaction with the wire, and the fluid dynamics of the free surface flow on the forming table. With most forming sections, one can immediately see the narrow SS that form near

the slice. These SS are 1/2 to 4 inches wide and correspond to the small-scale secondary flows emanating from the tube jets inside hydraulic headboxes or the wake of holes in the slice rectifier roll.

In order to analyze the dynamics of SS in the forming jet, we use a time-line projection imaging method. Events occurring in a fixed section of space are collected and assembled sequentially along a time line for analysis. This is shown in **Fig. 9** where we have reconstructed the images of the forming jet over an area of 0.6 by 6.2 inches at 1 inch from the slice over a period of 30 milliseconds in time.

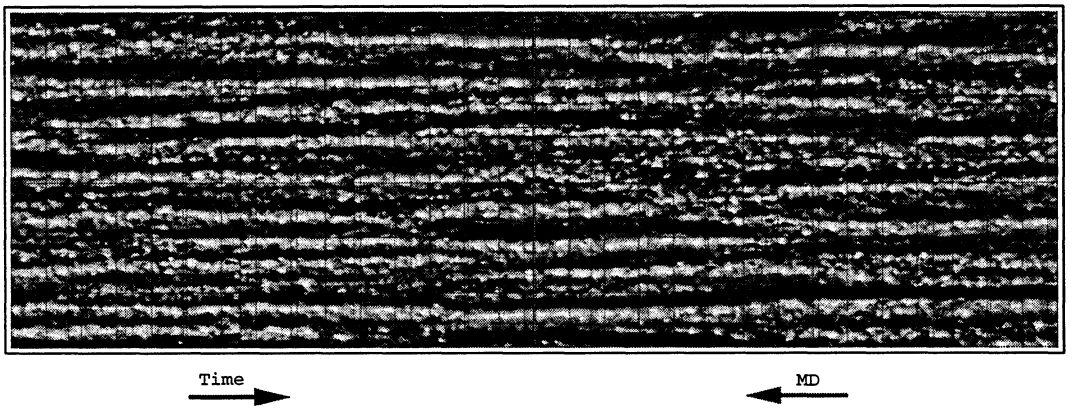


Figure 9: Time-line projection of the forming jet at 1 inch from the slice showing the dynamics of streaks delivered from the headbox.

This figure shows 30 sections outlined by red lines. The distance between adjacent red lines is 0.6 inch. The blue lines show a 1-inch square grid representing the length scale of the image. The images are taken at 1000 frames per second and each frame has an exposure time of 50 $\mu S$. Each 0.6-inch section, outlined by the red lines, represents the image of the same location of the forming jet (i.e., at 1 inch from the slice). Since the forming jet is moving on average at 3000 fpm or 0.6 inch per millisecond, the 0.6-inch sections move by exactly 0.6 inch in MD at each millisecond. The time line in **Fig. 9** covers 30 images of the 0.6-inch sections from time 0 to time 30 milliseconds stacked in sequence from top to bottom. Time-line images up to several seconds can be constructed for analysis of the forming jet dynamics.

The physics and dynamics of the forming jet delivered by the headbox can be analyzed with these time-line images, as shown in **Fig. 9**. Considering that in this headbox, the spacing between the tubes in each row is about 1 inch and the tubes have a staggered pattern, and considering the average SS width in **Fig. 7** and **9**, one can state with some confidence that SS are due to the secondary flows from the jets delivered from individual tubes in the tube bank. In **Fig. 9**, we see the effect of jets interacting from adjacent tubes. Careful analysis of these time-line images shows that the jets from adjacent tubes from two rows (i.e., $\sim$ 0.5 inch apart in CD) interact and compete with each other to leave a SS in the forming jet. Through this interaction, SS are deflected sideways. The interaction and subsequent deflection of the tube jets in the headbox result in sideways flapping-like motion of SS in the forming jet. The sideways motion of SS in the forming jet have significant impact on the small-scale fiber orientation and formation in the sheet. In fact, we believe that the small-scale variations in fiber orientation are caused by the local dynamics of SS in the forming jet.

Although here we have only presented the images of the top of the forming section, we note that SS should be viewed in terms of secondary flows throughout the forming jet. Similar SS exist at the underside of the forming jet. Interaction of these SS with the wire determine the structure of the sheet.

In the next subsection, we discuss the relation between the dynamics of SS in the forming section with the small-scale physical properties of the sheet.

### 3.6 The Impact of the Streak Dynamics on Small Scale Physical Properties

We can approximate the variation in angle of the forming jet SS with MD from the time-line images in **Fig. 9**. If the distance from the tube outlet to the slice is 29 inches and the distance from the slice to the impingement line is 6 inches, then for every 0.1 inch that a SS moves in CD of **Fig. 9**, the angle of the SS changes roughly by $\tan^{-1}(0.1/30) = 0.2$ degrees. Considering that fiber orientation is governed by the direction (or angle) of the velocity field relative to MD in the forming layer, this variation in the local forming jet angle would

result in significant fiber misalignment and fiber orientation nonuniformity over a small CD length scale. The magnitude of the variation would depend on the forming jet angle and the rush/drag ratio (i.e., the shear rate in the forming layer). We predict that the length scale of the in-plane average fiber orientation variation in the first layer from the wire side would be in the order of the length scale of SS in the forming jet.

Jet/wire interaction and the evolution of SS along the forming section have significant impact on the small scale basis-weight and moisture profile. The mechanism and interaction between the layer on the forming section and the formation characteristics on the wire are currently under study.

In order to eliminate the nonuniformities in physical properties caused by SS in the forming section, we need to eliminate the small-scale secondary flows induced by the tube jets inside the headbox.

# 4 Streak/Wave Analysis on the Forming Table

## 4.1 Schematic of a Drainage Model

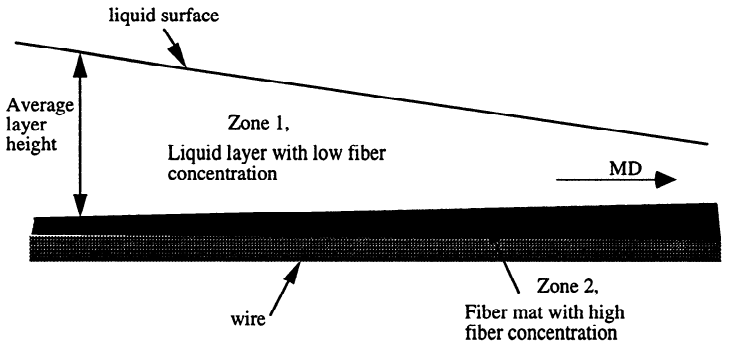


Figure 10: A simple drainage model showing the two different liquid layer zones on the forming wire.

Consider the drainage model on the forming table outlined in **Fig. 10**. Zone 1 has the same fiber concentration as the liquid inside the headbox, whereas Zone 2 has much higher concentration (~5 to 7 percent). The dry line forms at the point along MD where Zone 2 has completely drained. The shape of the dry line, visible on most forming tables, depends on the CD variations in the thickness of Zone 1. If Zone 1 has nonuniform thickness in CD, then the dry line becomes streaky, as demonstrated schematically in **Fig. 1**. Wet streaks are regions at the dry line which contain more liquid with low concentration (headbox level, approximately) of dispersed fiber than the rest of the layer (see **Fig. 1**). Assuming that the fibers are uniformly dispersed, this results in variation in mass density of the fibers in the sheet. Also, since the streaks contain more liquid, the moisture content and drying rate vary according to the width of the streaks. In most cases, the streaks result in detectable basis weight variations in the sheet. The length and the width of the streaks are important factors in the overall effect on nonuniform physical properties. A very short or narrow streak has no detectable effect on the physical characteristics. In contrast, long and relatively wide streaks result in detectable and often troublesome nonuniformities.

As mentioned earlier, SS on the forming table are caused by nonuniform or secondary flows in the headbox, the jet interaction with the wire, and the fluid dynamics of the free surface flow on the forming tables. With most forming tables, one can immediately see the narrow streaks that form near the slice. These streaks are 1 to 5 cm wide and correspond to the jets emanating from the tubes inside hydraulic headboxes or the wake of the holes in the slice rectifier roll. The streaks at the dry line are 0.2 to 0.5 m wide, depending on the headbox and the forming section design and flow parameters.

In order to eliminate the nonuniformities in physical properties caused by wet streaks in the forming section, we need to understand the origin of streak/wave formation and the physical mechanism of their evolution on the forming table to the relatively wide structures at the dry line. In the following subsection, we explain the physics of wave/streak formation and evolution on the forming table.

## 4.2 Fourier Analysis of Wet Streaks

The wave analysis is based on the spectral decomposition of the liquid surface height near the slice and computation of the wave evolution on the wire from the slice to the dry line. The purpose of this analysis is to explain the physical mechanism of the evolution of the apparently narrow streaks near the slice to the relatively wide streaks (0.2 to 0.5 m) at the dry line.

To analyze the evolution of the waves on the forming table, we use a filtration model of paper forming on the table, as demonstrated in **Fig. 10**. We distinguish two zones on the wire. One, where the fiber mat is forming on the wire, and the second zone where the liquid has a low concentration of fiber equal to that of the headbox. The analysis takes the amount of the drainage rate measurements to compute the average height of Zone 1. The waves or streaks are variations in the height of Zone 1 in the cross-machine direction.

Since the wave amplitude is smaller than the wavelength of the range of streaks that we are concerned about, one can show that in this case, the convective terms in the momentum equation are much smaller than the other terms. Therefore, for this application, the

momentum equation can be reduced to

$$\rho\frac{\partial\vec{u}}{\partial t} = \nabla p + \nabla\cdot[2\bar{\mu}D_{ij}] \tag{1}$$

where $\vec{u}$ and $p$ are the velocity vector and the pressure, respectively, $\rho$ is the density of the liquid, $D_{ij}$ is the rate of increase of strain, and the viscosity term $\bar{\mu}$ is the sum of dynamic, effective viscosity of fiber suspension and turbulent viscosities, i.e.,$\mu_{eff} + \mu_t$. We use the Prandtl's mixing length theory, given by

$$\mu_t = \rho l[2D_{ij} : \nabla\vec{u}] \tag{2}$$

where, $l$ is the mixing length (i.e., Eq. 28 which appears in a later section) and

$$D_{ij} = \frac{1}{2}\left(\frac{\partial u_i}{\partial x_j} + \frac{\partial u_j}{\partial x_i}\right). \tag{3}$$

Because of conservation of mass and the incompressibility condition, the velocity vector is a divergence-free function.

The height of the fluid surface defined as, $\zeta$, is expanded in terms of Fourier modes, as

$$\zeta(x,y) = \sum_{n=1}^{N}\frac{k_n}{\alpha_n}[G]\exp\left(ik_n x + \alpha_n\frac{y}{U}\right) \tag{4}$$

where

$$G = A_n[\exp(k_n\bar{\zeta}) - \exp(-k_n\bar{\zeta})] + iC_n[\exp(l_n\bar{\zeta}) - \exp(-l_n\bar{\zeta})] \tag{5}$$

and

| | |
|---|---|
| $\alpha_n$ | is the nth mode wave amplitude; |
| $\lambda_n$ | is the nth mode wave length; |
| $\zeta$ | is the layer thickness on the wire (height functions); |
| $k_n$ & $l_n$ | are the nth mode wave numbers ($k_n = 2\pi/\lambda_n$ and $l_n^2 = k_n^2 + \alpha_n/\bar{\nu}$); |
| $\bar{\nu} = \nu_{eff} + \nu_t$ | is the sum of the kinematic viscosity of the fiber suspension plus the eddy viscosity; |
| $A_n$ & $C_n$ | are constants which depend on the nth mode initial disturbance amplitude; |
| $\bar{\zeta}$ | is the average layer thickness (varies due to drainage along the table); |
| $x$ & $y$ | are cross-machine(CD) and machine direction(MD), respectively. |

The free surface conditions are the balance of tangential and normal stresses along with the dynamic condition at the free surface which constrains the free surface to a material surface, as it physically is.

The expanded series is substituted in the governing equations, and using the free surface conditions, the relation for the coefficients of the modes is derived. This relation is in the form of a set of nonlinear algebraic equations which are solved using the nonlinear equation solver in IMSL.

The relation between the exponential growth rate, $\alpha_n$, and the wavelength, $\lambda_n$, or the wave number, $k_n$, is given by a nonlinear algebraic equation:

$$F(\alpha_n,\ k_n;\ \bar{\nu},\ \hat{\varpi_\circ},\ \bar{\zeta}) = 0 \tag{6}$$

where

$\nu_{eff} = \nu\left[1 + \frac{6}{5} r_p^2 \phi\left(\eta_T + 2\bar{\eta} + 2\eta_\perp\right)\right]$ ·····[23]

| | |
|---|---|
| $\nu$ | is the viscosity of white water; |
| $r_p$ | ratio of the fiber length to diameter; |
| $\phi$ | is the fiber volume fraction; |
| $\eta_T, \bar{\eta}, \& \eta_\perp$ | are functions of $r_p$; |
| $\hat{\varpi_\circ} = \sqrt{Gk_n + \frac{\sigma k_n^3}{\rho}},\ G = g + \varpi_\circ$ | |
| $\varpi_\circ$ | is the drainage rate on the wire; |
| $g$ | is gravity; and |
| $\sigma$ | is the surface tension of the fluid. |

### 4.3 Results

By calculating the growth and decay rates of the waves in the machine direction, $y$, along the forming wire, we compute the surface height of the liquid along the full forming table. Note that the results are functions of several parameters on the forming wire including the drainage rate, the kinematic and turbulent viscosities, the average layer height, the machine turbulent viscosities, the average layer height, the machine speed, and the location of the drainage element. Therefore, the growth and decay rates for each mode vary along the forming table. The streaks at the slice have a broad spectrum of wavelengths ranging from a few centimeters to more than a meter. The characteristic length scale of the streaks at

the dry line are determined by the critical mode which becomes dominant as the streaks are evolving on the forming table. The reason for this is that the modes with smaller wavelengths grow and decay very rapidly before they reach the dry line. The streaks with larger wavelengths take too long to grow and, therefore, they are of no consequence. **Fig. 11a** and **11b** show the growth and decay rates of the waves at a given MD location on the wire. Only the critical mode grows to its maximum amplitude just in time to reach the dry line and form the dry-line streaks.

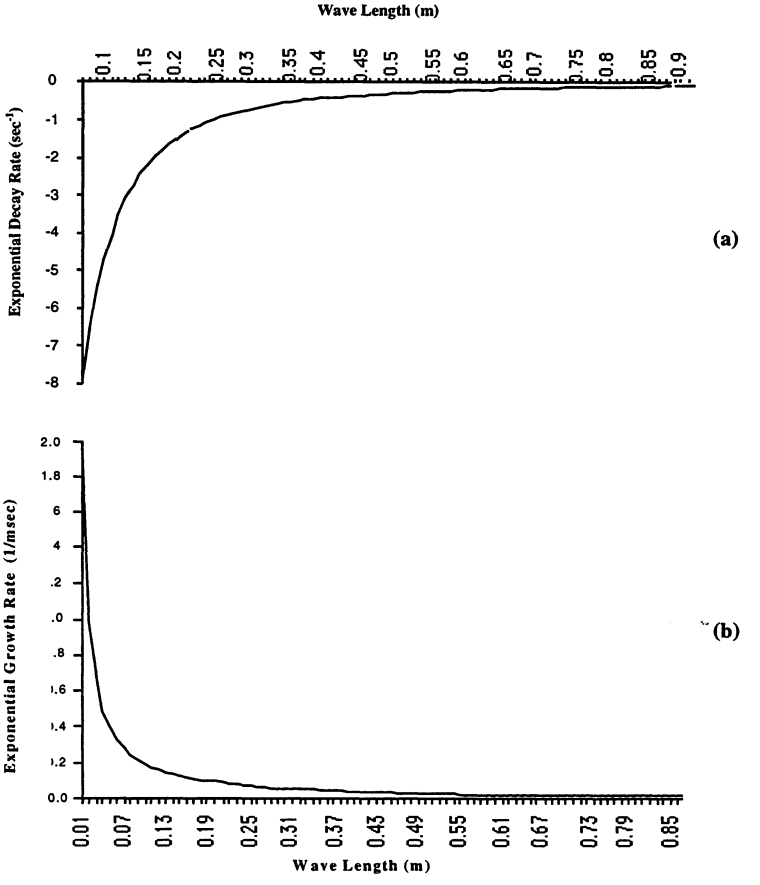


Figure 11: Rates of growth and decay of streaks on the forming table
(a) Decay of streaks (b) Growth of streaks

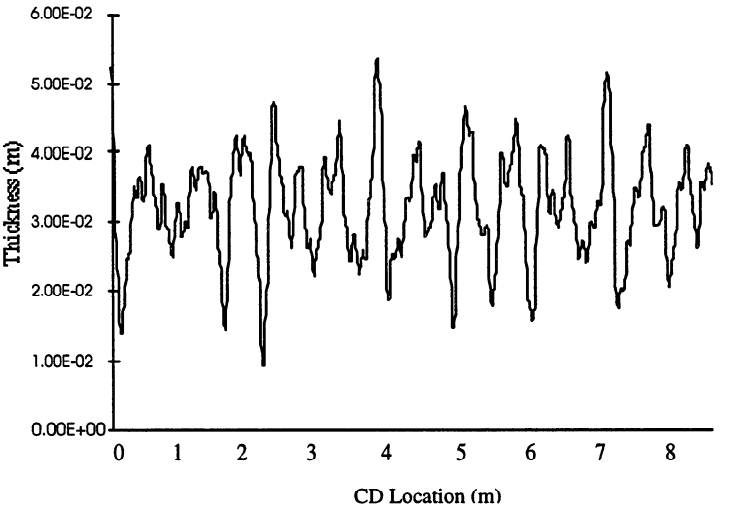


Figure 12: Computation of surface height across the machine at about 6′ from the slice

For the headbox and the forming table considered in this study, the wave amplitudes on the wire near the slice and at about 2 m from the slice are plotted in **Fig. 12**. Note that the streaks quickly evolve to the dominant mode which in this case is about 0.45 m wide. The measurements of the layer thickness on the wire at the same thickness from the slice show good qualitative agreement with the calculations.

The streaks that are computed at the dry line have the same 0.4 to 0.5 m width as observed on the machine. Also, the results show the same qualitative length scale of fluctuations as found in the ZD ultrasound measurements presented in [17].

# 5 Effect of Secondary Flow on Fiber Orientation

## 5.1 Two Types of Secondary Flow

Secondary flows in a headbox are weak, three-dimensional flow patterns that superimpose on the basic or primary two-dimensional flow due to hydrodynamic effects alone. These secondary patterns have small velocity components in the CD. Although the magnitude of the CD velocity components is small compared with the MD velocity, its effect on fiber orientation is significant. Cross-flows originating in the headbox result in nonuniform shear on the wire in the CD. Considering that the shear stress on the wire is the main factor determining fiber orientation, the secondary flows inside the headbox have profound influence on the average fiber angle. This causes nonuniform fiber orientation in the CD.

Two kinds of secondary flows could occur in the headbox. The first kind results from flow retardation due to boundary layer formation at the side wall of a converging channel. Examples of secondary flow induced by boundary layers at side walls occur in various hydrodynamic systems [24]. The second kind of cross-flow is from the anisotropy in turbulent Reynolds stresses. A discussion follows later.

Consider a straight rectangular channel. Here, the simple geometry of the channel provides one type of fluid problem. It is possible to isolate the physics of the formation of secondary flows of the second kind [25,26] from other cross-flow generating effects. In this geometric configuration, the structure of turbulent fluid motion is the sole generator of the secondary mean flows. The weak secondary flow is in a plane normal to the streamwise axis of the channel. Its magnitude is approximately 1–3% of the main flow. This flow configuration also provides the opportunity to develop and test turbulent closure models, considering the correct and accurate simulation of secondary currents [27,28].

Recent investigators [29,30] have presented direct numerical simulations (DNS) of low Reynolds number turbulent flows in straight channels. These simulations provide a database from which it is possible to calculate the turbulent velocity and pressure correlations. The computed instantaneous velocity field near the channel will capture the bursting events also observed in some experiments [31-33]. Averaging the flow field in both the streamwise

direction and in time provides mean flow streamwise velocity and secondary velocity distributions. Ejection structures produced during bursting events create streamwise vortices [29]. Near the corners, the reduced mean shear prohibits the occurrence of ejections. Meanwhile, there are strong ejections along the walls away from the corners. This distribution of ejections is the major contributor to the anisotropy of the normal Reynolds stresses. It also generates the mean secondary circulations carrying streamwise momentum from the core of the channel towards the corners. The earlier investigators also observed a nonlinear interaction between simultaneous ejections produced along perpendicular walls near a corner [29]. This interaction results in the redistribution of turbulent intensities there.

Simulating flow problems of technological interest with DNS is beyond the scope of currently available computers. For example, to achieve a sufficient spatial resolution for the turbulent channel flow, Gavrilakis [30] had to use 16.1 million grid nodes and more than 60 days on a supercomputer for one run. One must, therefore, rely on a turbulence model that can correctly account for the anisotropies in a more realistic computational time. Speziale [28] evaluated different turbulent closure models. He suggests the application of the two-equation, nonlinear $\kappa - \epsilon$ method for engineering calculations. An advantage of this method compared to the linear (standard) $\kappa - \epsilon$ method is the more accurate prediction of the turbulent channel flows. The consequence is better turbulent secondary flow prediction. The derivation used an asymptotic expansion subject to the constraints of dimensional and tensorial invariance and realizability [34]. This model obtains the turbulent kinetic energy, $\kappa$, and dissipation rate, $\epsilon$, from a modeled version of transport equations [34,35]. These are the same form as those used in the linear $\kappa - \epsilon$ method. The closure formulation for the Reynolds stress tensor, $\tau^t$, takes a simple non-linear representation introducing new quadratic terms in the mean velocity gradients. This formulation is similar to the constitutive equation of dilute polymers. It contains two more constants compared with the linear model. Speziale [34] concludes that future research is necessary to obtain a more detailed picture of the turbulent structure in rectangular channels predicted by the nonlinear model.

Colombini [36] applied the nonlinear $\kappa - \epsilon$ method in the linear stability analysis of the formation of longitudinal ridges. In straight, infinitely wide channels, the free surface tur-

bulent flow over a deformable and erodible bed is unstable to transverse disturbances with a wavelength equivalent to the flow depth. The nonlinear $\kappa - \epsilon$ model has been successful in modeling the turbulence-driven, cellular secondary motions directed to amplify the bed perturbations. The interactions of the flow and the erodible bed thus lead to the formation of longitudinal ridges even without side walls.

Nezu *et al.* [37] have studied secondary currents in straight channel free surface flows of different aspect ratios. They address the initiation and maintenance mechanism of cellular secondary currents in a straight, wide channel with a flat solid bed. They concluded that secondary currents appear only near the side walls. If the ratio of width to depth, B/h, is greater than 4, there are no cellular secondary flows in the central region of the channel. Numerical simulations of other investigators [38] agree with these findings. Our work will systematically evaluate the effect of aspect ratio in confined and free surface flows.

Here, we consider the analysis of secondary flows and their effects on fiber orientation. The following subsections outline the governing equations and the methods applied in the numerical simulations. Applications to the headbox hydrodynamics focusing on the secondary flows of the first and second kind are in the following subsections. This section concludes with a brief summary of present results.

## 5.2 Governing Fluid Flow Equations

The following momentum conservation and continuity equations govern the flow of an incompressible and homogeneous viscous fluid:

$$\rho\left(\frac{\partial \vec{u}}{\partial t} + \vec{u} \cdot \nabla \vec{u}\right) = -\nabla p + \rho g + \nabla \cdot \tau \tag{7}$$

$$\nabla \cdot \vec{u} = 0 \tag{8}$$

where

$\vec{u}$ = $u_i = (u,\ v,\ w)$ = instantaneous fluid velocity vector,
$p$ = pressure,
$g$ = gravitational acceleration or body force per unit of mass,
$\rho$ = density, and
$\tau$ = $2\bar{\mu}D_{ij}$ = fluid stress tensor, where $D_{ij}$ is the rate of increase of strain (Eq. 3).

For a Newtonian fluid with constant viscosity, the last term in the momentum conservation

equation is the following:

$$\nabla \cdot \tau = \mu \nabla^2 \vec{u} \tag{9}$$

where

$\mu$ = dynamic viscosity of the fluid.

In a turbulent flow, the velocity and pressure field decompose into ensemble mean and fluctuating parts, respectively, as the following shows:

$$\vec{u} = \bar{\vec{u}} + \vec{u}' \tag{10}$$

$$p = \bar{p} + p'. \tag{11}$$

In this equation, the overbar denotes the ensemble mean and the prime denotes the fluctuating components. Figure 13 shows the mean and fluctuating velocity components in time for steady and unsteady flows, respectively.

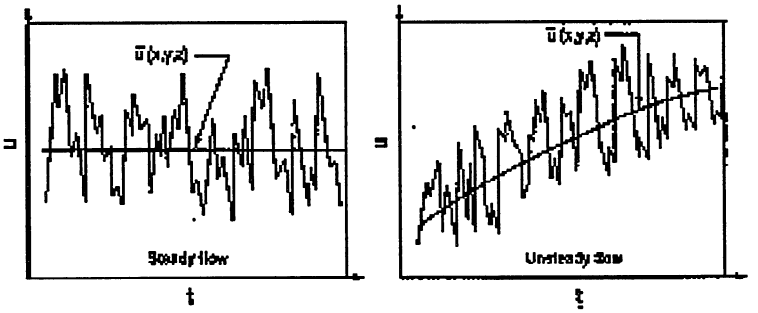


Figure 13: Fluctuating and mean velocity components in steady and unsteady flows.

After substituting Eqs. 9 and 10 into Eq. 7 and averaging Eq. 7 in time, the governing equation of a turbulent flow reduces to the following:

$$\rho\left(\frac{\partial \bar{\vec{u}}}{\partial t} + \bar{\vec{u}} \cdot \nabla \bar{\vec{u}}\right) = -\nabla \bar{p} + \rho g + \nabla \cdot \hat{\tau} \tag{12}$$

$$\nabla \cdot \bar{\vec{u}} = 0 \tag{13}$$

In Eq. 12, the stress tensor, $\hat{\tau}$, includes both the viscous and turbulent Reynolds stress tensors, such that the following equation is true:

$$\nabla \cdot \hat{\tau} = \mu \nabla^2 \bar{\vec{u}} + \nabla \cdot \tau^t \tag{14}$$

The following equation provides the components of the Reynolds stress tensor [39], $\tau^t$:

$$\tau_{ij}^t = -\rho u_i' u_j'. \tag{15}$$

The Reynolds stress tensor, $\tau^t$, introduces additional unknowns for a turbulent flow problem governed by Eq. 12. To describe the mean velocity and pressure fields, a closure formulation is necessary to relate the components of the Reynolds stress tensor to the mean flow velocity or velocity gradients. Without a closure formulation, DNS can theoretically solve the Navier-Stokes equations–Eq. 7 combined with Eq. 9–to obtain the instantaneous velocity and pressure fields. This task demands a very fine space discreatization, however. It is not a practical approach for many industrial problems.

### 5.3 Numerical Method

To calculate secondary flows of the first kind, one can apply the standard, linear $\kappa - \epsilon$ model for closure of the averaged momentum equation, Eq. 12. Any numerical method to obtain the second kind of secondary currents in confined and free-surface flows should consider the anisotropy of the turbulent field. The computational method for these calculations uses the volume-of-fluid (VOF) computational technique [40,41]. Original development of this technique was for both confined and free-surface flows. Our work extends its application from laminar to turbulent flows employing a nonlinear $\kappa - \epsilon$ described below.

McKibben and Aidun [40,41] described the VOF solution of the governing equations, i.e., Eq. 7 with Eq. 9 or Eq. 12 with Eq. 14. There has been modification of their numerical method with the introduction of implicit shear stress calculation and the advancement of the advection terms using the Adam-Bashforth scheme. These modifications enhance the efficiency of the numerical simulations [42]. Other researchers have used similar numerical techniques [30,43].

This subsection summarizes the steps of a cycle in the VOF procedure. In describing this time-splitting method, the overbars are eliminated, and the procedure is applicable for both turbulent and laminar flows with the inclusion of an appropriate closure for the stress terms.

**First step**: The initial procedure is to calculate an intermediate or provisional $\tilde{\vec{u}}$ velocity

field using the following equation:

$$\hat{\vec{u}}^n = \vec{u}^n + \frac{\Delta t}{2}(-3\vec{u}^n \cdot \nabla \vec{u}^n + \vec{u}^{n-1} \cdot \nabla \vec{u}^{n-1}) + \Delta t(-\frac{\nabla p^n}{\rho} + g) + \frac{\Delta t}{2} \frac{[\nabla \cdot \hat{\tau}(\vec{u}^m) + \nabla \cdot \hat{\tau}(\hat{\vec{u}}^m)]}{\rho} \quad (16)$$

In this equation, the superscripts $n$ and $n-1$ denote values calculated in previous $n$ and $n-1$ cycles. The superscripts $m$ and $m-1$ refer to the iterative nature of the solution of Eq. 16. $\Delta t$ is the time increment, and $\tau(\cdot)$ symbolizes a functional relation and closure for the stress calculation.

**Second step**: One next applies the continuity constraint to obtain the Poisson equation for pressure:

$$\Delta t \nabla \cdot \nabla \partial p = \nabla \cdot \hat{\vec{u}} \quad (17)$$

where

$\partial p$ = the pressure change needed to satisfy mass conservation.

**Third step**: Using the following equations, one next updates the pressure and velocity fields:

$$p^{n+1} = p^n + \partial p \quad (18)$$

$$\vec{u}^{n+1} = \hat{\vec{u}} - \Delta t \nabla \partial p \quad (19)$$

Earlier work [40,41] details the space discreatization of the different terms in Eq. 16-19 on a staggered grid. They also describe the boundary conditions for the Navier-Stokes equation and the solution of the pressure Poisson equation, Eq. 17. There has been extensive testing of the code for laminar, free-surface and confined-flow benchmark problems.

The current study proposes the inclusion of a nonlinear $\kappa - \epsilon$ model to this code to capture the secondary flows of the second kind induced by turbulent flow. The finite element method in a fluid dynamics analysis package [44] solves the standard (linear) $\kappa - \epsilon$ model. This provides the secondary flows of the first kind presented in this paper for confined flow in a headbox.

## 5.4 Headbox Secondary Flows Due to SideWalls

This subsection focuses on the secondary flow of the first kind. This is the main cause of nonuniform fiber orientation in CD. **Table 1** provides the specifications for the full-scale headbox considered in this work. Figure 14 is a diagram showing the headbox and an individual tube, and **Fig. 15** shows the geometry and the computational grid.

Since the solution for the governing equations is in nondimensional form, the results are also nondimensional. The length scale is the size of the box inlet, and the velocity scale is the inlet velocity of the fluid into the box. **Table 2** offers a conversion for the dimensionless members in the figures to dimensional quantities for the case of 45,000 gal/min total flow rate through a headbox with a 1.5in. slice opening. Here the average forming jet speed will be 2400 ft/min with a higher or lower machine speed, depending on the rush or drag mode of operation.

Since the boundary conditions and the geometry considered in this study are symmetrical in the Z or MD plane of the headbox, we present the results for half the box. The result for the full box is a mirror image projection for the other half.

Table 1: **Headbox parameters and flow conditions**

| Parameters | Dimensional | Dimensionless |
|---|---|---|
| Width | 300 in. | 20 |
| Inlet height | 15 in. | 1 |
| Total flow rate | 45,000 gal/min | |
| Slice opening, B | 1.5 in. | 0.1 |
| Average jet velocity | 2,400 ft/min | 10 |
| No vanes | | |
| No side ejection | | |

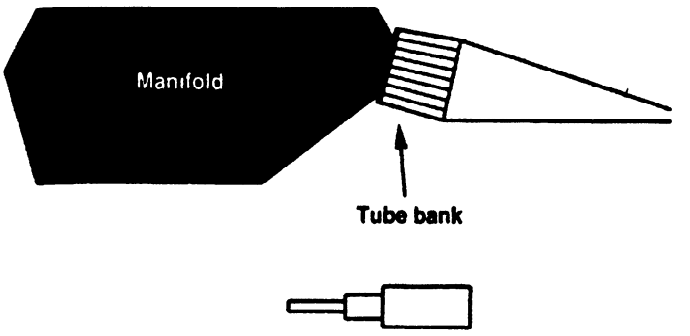


Figure 14: Schematic of a headbox and an individual tube

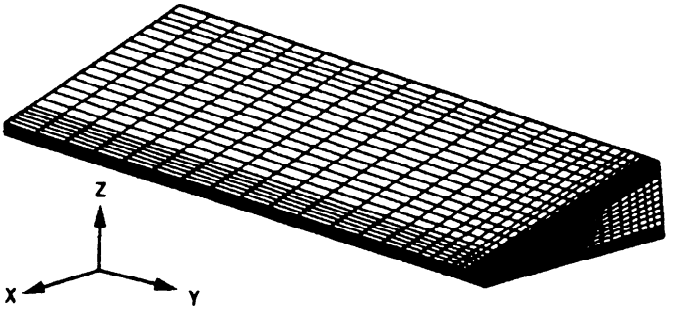


Figure 15: The geometry and computational grid system for the headbox

Table 2: **Conversion factor for nondimensional to dimensional units**

| To convert | To dimension | For the case of 45,000 gal/min and 1.5 in. slice multiply by |
|---|---|---|
| Length | m (ft) | 0.381 (1.25) |
| Velocity | m/s (ft/min) | 1.22 (240) |
| Pressure | $N/m^2$ (psi) | 1488 (0.216) |

## 5.5 Uniform Inflow

Consider first the case with uniform pressure at the inlet to the box. Figure 16 shows the resulting pressure contour lines in the symmetry plane. As expected, the contour plots show that pressure decreases as the fluid accelerates through the box. The pressure contour lines become denser near the outflow. This indicates sharper decrease in pressure (larger pressure gradient) due to the rapid velocity increase toward the channel exit. Figure 17 illustrates a velocity vector plot. These plots only show a cross section of the headbox. To learn more about the global features of the flow, it is necessary to examine the pressure variations in the CD.

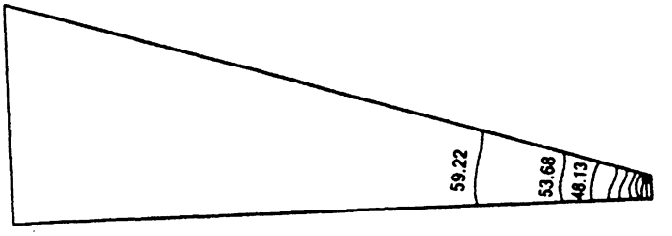


Figure 16: Pressure contour plot at the middle cross section of the symmetry plane

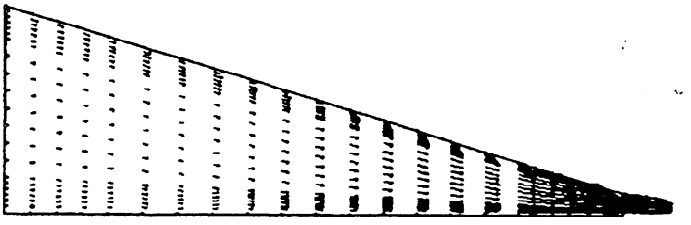

Figure 17: Velocity vector plot at the middle cross section of the symmetry plane

To investigate the pressure distribution in the headbox, Figure 18 provides the pressure contour plots on the inner surface showing a three-dimensional view of pressure on the boundaries of the headbox. Figure 19 shows the pressure contours or isobars in a horizontal plane located in the middle of the slice. Although the boundary conditions are uniform in the CD, the isobars show that the variation in the pressure field is three dimensional. The

pressure changes in both the CD and the MD.

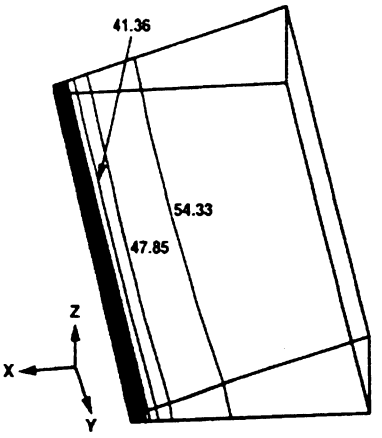


Figure 18: Pressure contour plot on the boundaries of the headbox

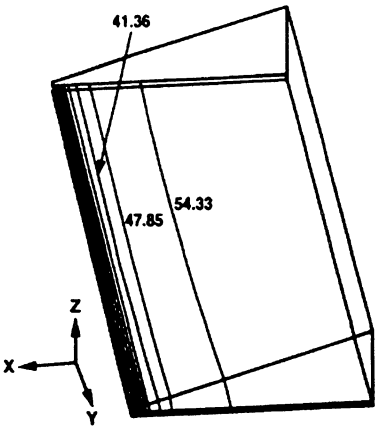


Figure 19: Top view of the pressure contour plot at the horizontal plane intersecting the middle of the slice

For quantitative information, one can compare the magnitude of the pressure variation at various levels of the slice presented in Figure 20 to the plot of the MD pressure drop shown in Figure 21. The pressure variation in CD is primarily due to the retardation of velocity near the sidewall. Our objective was to study the generation and features of cross flows because of their effects on fiber orientation. It was therefore important to examine the influence of CD pressure variation on the flow. We wanted to see if the CD pressure gradient generated

finite cross-flow.

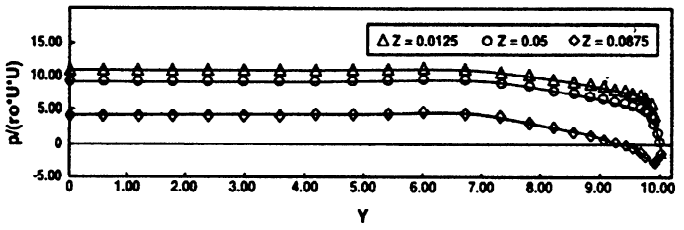


Figure 20: CD pressure variation in the headbox at the slice ($r_o$ is fluid density, U is characteristic inflow velocity)

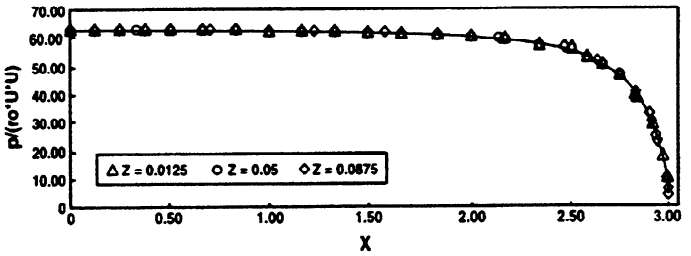


Figure 21: MD pressure drop along the axis of symmetry

To address this question, it was necessary to examine the CD(or y) component of velocity(v) inside the headbox. The contour plots of v shown in Figures 22 and 23 clearly indicate a local minimum near the sidewall. The values of this local minimum is small compared to the positive value of the cross-flow velocity. Figure 22 illustrating the distribution of the y-component of velocity in the slice also indicates this. The relative magnitude of the cross-flow velocity components is the critical factor in generation of nonuniform fiber orientation. Figures 24 and 25 show the MD and CD components of velocity along a line in the middle of the slice, respectively. Besides the local minimum near the sidewall, these figures clearly indicate a positive cross-flow. This reaches a maximum at approximately 3.3 ft (1 m) from the sidewall of the headbox. Comparing the x- and y-components of velocity shows that the maximum cross-flow is approximately 1% of the x-component of velocity. Generation of the cross-flow is due to the converging section of the headbox in the x-z plane bounded by the vertical sidewalls. The boundary layer at the vertical sidewall retard the flow in the

streamwise direction. Mass conservation therefore force the flow to move in the CD.

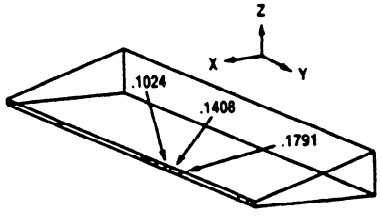


Figure 22: Contour plot of the y-component of fluid velocity in CD inside the headbox

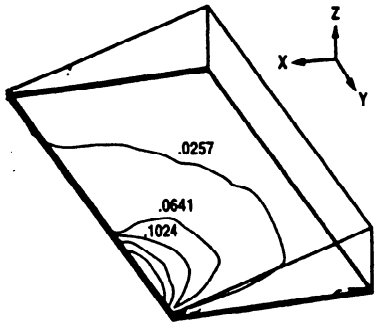


Figure 23: Top view of the horizontal plane intersecting the middle of the slice

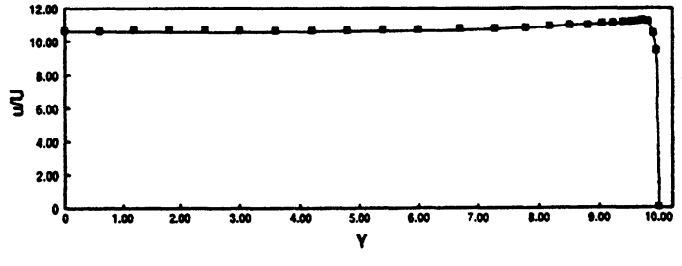


Figure 24: The x- or MD component of fluid velocity, u, at the middle of the slice

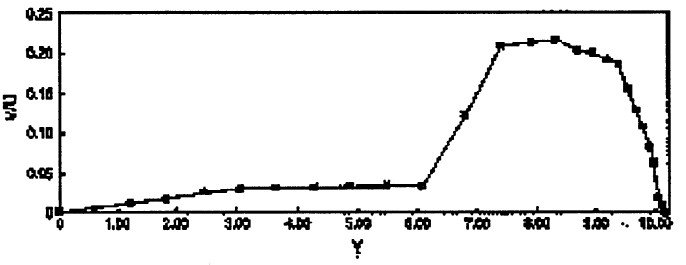


Figure 25: The y- or CD component of fluid velocity, u, at the middle of the slice

Even when a perfect pressure and flow rate distribution exists in the tube bank, these results emphasize that the flow inside the headbox will be three-dimensional because of the secondary flows. In addition, the results show the location of the maximum cross-flow.

Turbulent flow characteristics partly control the formation and flocculation. Figure 26 is a plot of the computed turbulent flow characteristics inside the headbox. The individual components of this figure present three-dimensional views of the turbulent kinetic energy, $\kappa$, dissipation, $\epsilon$, and turbulent viscosity, $\mu_t$. This figure shows a turbulent intensity in the headbox that is almost uniform. The only regions with large variations in turbulent kinetic energy, dissipation, and viscosity are near the solid walls of the converging channel. As one would expect, there are large velocity gradients here resulting in a more intense turbulent energy production and dissipation.

## 5.6 The Influence of Nonuniform Inflow on the Cross-flow at the Slice

Dividing the inlet into three sections as Figure 27 shows helps in examining the effect of nonuniform influx at the inlet to the headbox on the cross-flow at the slices. Figure 28 presents the cross-flow at the slice when the flux in section B is $\pm$ 10% of the flux in region A. The results show that the flux into the headbox has significant effect on the cross-flow at the slice. This result is consistent with the physical explanation of the nonuniform CD velocity by the retardation of the flow due to the sidewall. These results demonstrate that by computationally optimizing the influx, we can substantially reduce CD flow and fiber disorientation.

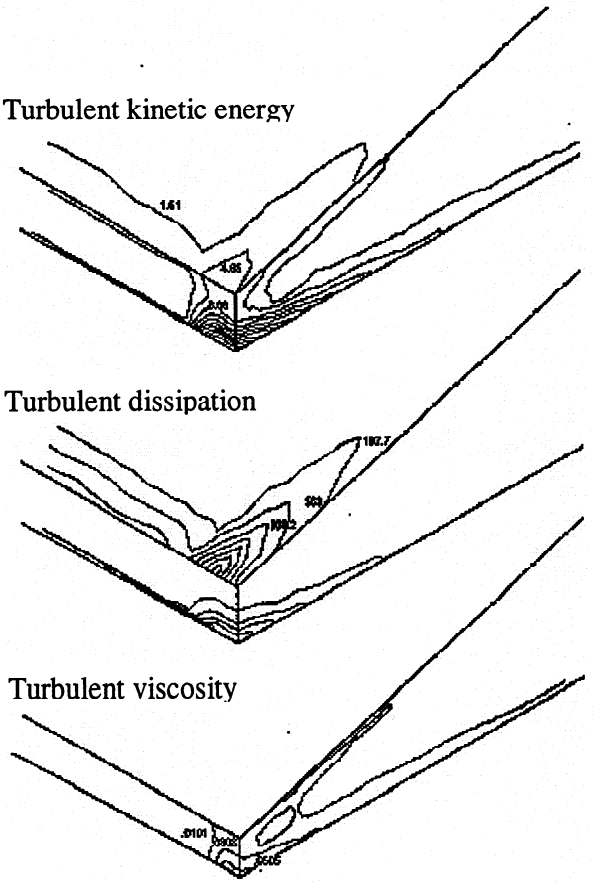


Figure 26: Three dimensional view showing turbulent kinetic energy, turbulent dissipation rate, and turbulent(eddy) viscosity

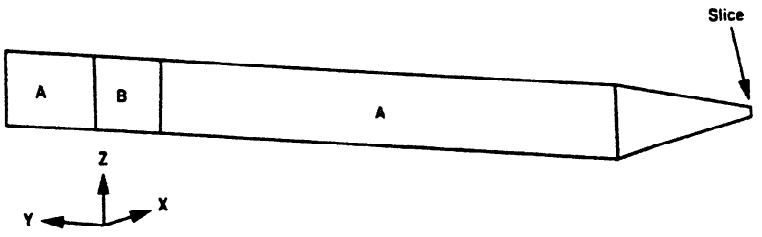


Figure 27: Schematic of regions showing variation in influx profile

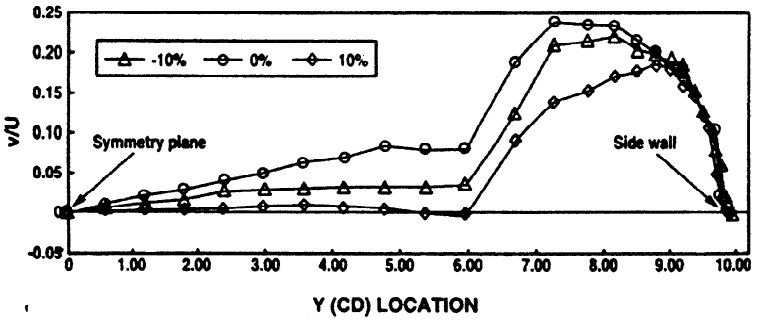


Figure 28: Variation of the CD velocity profile across the headbox

## 5.7 Secondary Flows Due to Turbulence Anisotropy

### 5.7.1 Origin of secondary flows of the second kind

To understand the formation of secondary currents in straight rectangular channels, it is necessary to transform the governing equations into a vorticity stream function formulation. This demonstrates the condition for the existence of a vorticity vector in the axial (main) flow direction. Figure 29 illustrates the geometry of a rectangular channel.

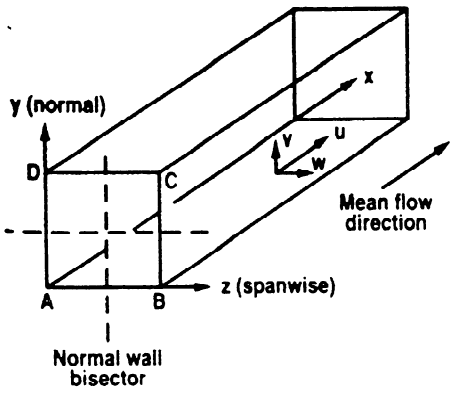


Figure 29: Geometry of a straight rectangular duct

Taking the x-direction to be the axial streamwise flow direction and assuming that the steady flow does not change in this direction provide the following set of equations:

$$\rho\left(\bar{v}\frac{\partial\bar{u}}{\partial y}+\bar{w}\frac{\partial\bar{u}}{\partial z}\right)=-\frac{\partial\bar{p}}{\partial x}+\rho g_x+\mu\nabla^2\bar{u}+\frac{\partial\tau^t_{zx}}{\partial z}+\frac{\partial\tau^t_{yx}}{\partial y} \tag{20}$$

$$\rho\left(\bar{v}\frac{\partial\omega_x}{\partial y}+\bar{w}\frac{\partial\omega_x}{\partial z}\right)=\mu\nabla^2\omega_x+\frac{\partial^2(\tau^t_{yy}-\tau^t_{zz})}{\partial y\partial z}+\frac{\partial^2\tau^t_{zy}}{\partial z^2}-\frac{\partial^2\tau^t_{zy}}{\partial y^2} \tag{21}$$

$$\nabla^2\Psi=\omega_x \tag{22}$$

$$\bar{v}=\frac{\partial\Psi}{\partial z} \tag{23}$$

$$\bar{w}=-\frac{\partial\Psi}{\partial y} \tag{24}$$

where

$\omega_x$ = axial vorticity
$\Psi$ = stream function

Speziale [45] provides the derivations for Eqs. 20-24. On the right hand side of Eq. 21, the vorticity equation, the terms formed from the Reynolds stress components represent the source term for vorticity production. If the difference of the normal Reynolds stresses equals zero, i.e., $\tau^t_{yy}=\tau^t_{zz}$, then no generated vorticity results. Then $\omega_x=\Psi=\bar{v}=\bar{w}=0$. In other words, no secondary flow can exist in the duct. This would contradict earlier experimental observations [46]. To model these flow phenomena numerically, the turbulent closure model must be able to predict the anisotropy of turbulent normal stresses.

Figures 30 and 31 present the instantaneous velocity field – ($u$, $v$, $w$) – in a straight duct calculated by DNS [29]. Figure 30 shows the streamlines of the main flow, and Figure 31 illustrates the instantaneous secondary flow vectors. Averaging the instantaneous streamlines of the main flow, $u$, and the secondary velocity vector field, $v$ and $w$, in time and along the duct axis provides the mean flow quantities. Figures 32 and 33 display these. Figure 32 shows the mean streamwise flow, $\bar{u}$. Due to the secondary flow circulations directed from the center of the duct toward the corners, these streamlines bulge along the corner bisectors. Figure 33 presents the mean secondary velocity field, $\bar{v}$ and $\bar{w}$, causing this bulging.

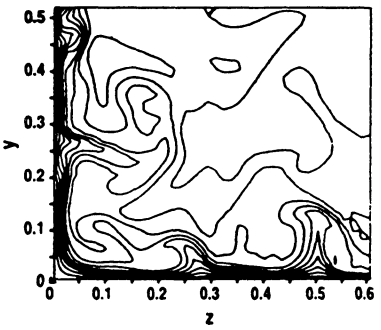


Figure 30: Instantaneous velocity field in the lower left corner of a straight duct showing main flow

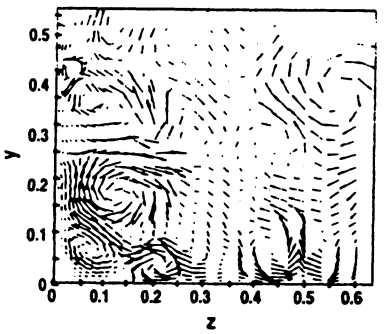


Figure 31: Instantaneous velocity field in the lower left corner of a straight duct showing secondary velocity field [29]

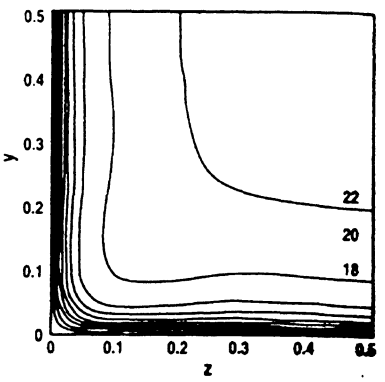


Figure 32: Ensemble mean velocity field in the lower left corner of a straight duct showing mean main flow

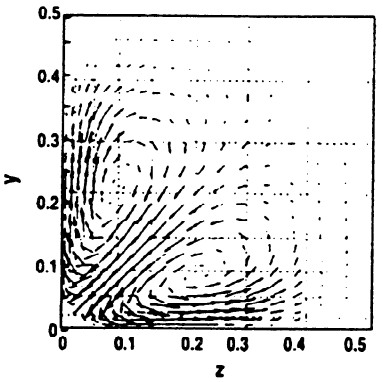


Figure 33: Ensemble mean velocity field in the lower left corner of a straight duct showing mean secondary velocity field [29]

### 5.7.2 Numerical modeling with the non-linear $\kappa - \epsilon$ method

In closing Eqs. 12 and 14, the non-linear $\kappa-\epsilon$ method provides a formulation that one would expect to simulate secondary flow currents. This formulation uses the secondary solution of two more transport equations that are identical to those of the standard (linear) $\kappa - \epsilon$ model.

The version of these equations in the present study comes from Speziale [34]. Eqs. 25 and 26 describe the transport of turbulent kinetic energy, $\kappa$, and dissipation rate, $\epsilon$, respectively:

$$\frac{d\kappa}{dt} = \frac{\tau_{ij}^t}{\rho}\frac{\partial \bar{p}\bar{u}_i}{\partial x_j} + C_1\frac{\partial}{\partial x_j}\left[\frac{\kappa}{\rho^2\epsilon}\left(\tau_{jm}^t\frac{\partial \tau_{ij}^t}{\partial x_m} - \delta\tau_{ij}^t\frac{\partial \kappa}{\partial x_j}\right)\right] - \epsilon \tag{25}$$

$$\frac{d\epsilon}{dt} = -\frac{C_2}{\rho}\frac{\partial}{\partial x_i}\left(\frac{\kappa\tau_{ij}}{\epsilon}\frac{\partial \epsilon}{\partial x_j}\right) + \frac{C_3\epsilon\tau_{ij}^t}{\rho\kappa}\frac{\partial \bar{u}_i}{\partial x_j} - \frac{C_4\epsilon^2}{\kappa}. \tag{26}$$

In these equations, $C_{(\cdot)}$ *et al.* are dimensionless constants.

In the lowest order nonlinear $\kappa - \epsilon$ model, it is possible to calculate the shear stress [34] using the following equation:

$$\tau_{ij}^t = -\frac{2}{3}\rho\kappa\delta_{ij} + \rho\kappa^{1/2}l\bar{D}_{ij} + C_D\rho l^2\left[\bar{D}_{im}\bar{D}_{mj} - \frac{1}{3}\bar{D}_{mn}\bar{D}_{mn}\partial_{ij}\right] + C_E\rho l^2\left[\tilde{D}_{ij} - \frac{1}{3}\tilde{D}_{mn}\partial_{ij}\right] \tag{27}$$

The following equations provide terms for this equation:

$$l = \frac{C\kappa^{3/2}}{\epsilon} \tag{28}$$

$$\bar{D}_{ij} = \frac{1}{2}\left[\frac{\partial \bar{u}_i}{\partial x_j} + \frac{\partial \bar{u}_j}{\partial x_i}\right] \tag{29}$$

$$\tilde{D}_{ij} = \frac{\partial \bar{D}_{ij}}{\partial x_j} + \bar{\vec{u}} \cdot \nabla \bar{D}_{ij} - \frac{\partial \bar{u}_i}{\partial x_k}\left[\bar{D}_{kj} - \frac{\partial \bar{u}_j}{\partial x_k}\bar{D}_{ki}\right] \tag{30}$$

In Eq. 27, the additional constants, $C_D$ and $D_E$, are necessary in comparison to the linear $\kappa - \epsilon$ method. Determination of these parameters comes from calibration with the help of experimental or DNS results.

Considering only the first two terms on the right-hand side of Eq. 27, one can obtain the shear stress formulation of the linear $\kappa - \epsilon$ method. Remembering this, note that the linear $\kappa - \epsilon$ model predicts the following for Eq. 21:

$$\tau_{zz}^t = \tau_{yy}^t = \tau_{xx}^t = -\frac{2\rho\kappa}{3} \tag{31}$$

The linear formulation consequently does not generate vorticity. In contrast to the linear model, the nonlinear method yields the following [34]:

$$\tau_{zz}^t \cong -\frac{2\rho\kappa}{3} + \frac{C_D \rho l^2}{4}\left(\frac{\partial \bar{u}}{\partial z}\right)^2 \tag{32}$$

$$\tau_{yy}^t \cong -\frac{2\rho\kappa}{3} + \frac{C_D \rho l^2}{4}\left(\frac{\partial \bar{u}}{\partial y}\right)^2 \tag{33}$$

Equations 32 and 33 satisfy the necessary condition for the development of the secondary flows, i.e., $\tau_{yy}^t \neq \tau_{zz}^t$. This justifies the choice of the nonlinear $\kappa - \epsilon$ method for the present study.

The simultaneous solution of Eqs. 25-30 with Eq. 12 provides the turbulent mean velocity and pressure fields. Figure 34 displays the secondary flow streamlines calculated by a simplified form of the nonlinear $\kappa - \epsilon$ method [34].

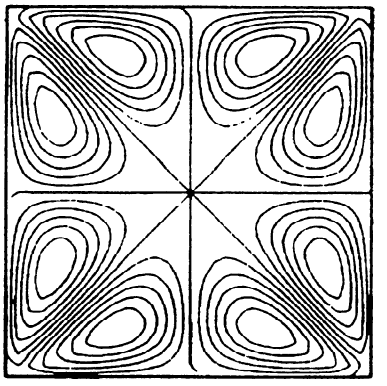

Figure 34: Mean secondary flow streamlines [34]

## 5.8 Summary

In principle, secondary flow in a hydrodynamic system is a weak stream with a more complex flow pattern superimposed on the primary flow pattern. In a headbox, the base flow is the two-dimensional flow pattern with zero CD velocity component. The secondary flows are weak three-dimensional flow patterns superimposed on the primary flow. The result is a three-dimensional flow pattern. The secondary flows that are important in this study are of two kinds:

- Type I: Secondary flow induced by the curvature in streamlines in the developing flow inside the headbox and the transverse velocity that satisfy the continuity condition
- Type II: Secondary flow caused by the anisotropy of turbulent flows.

We have identified these two types of secondary flow inside the converging section of the headbox. Such secondary flows result in nonuniform cross-flows in the headbox and at the slice. The secondary flow of the first type is due to the flow retardation at the slice resulting in misalignment of a section of the forming jet with the wire. The nonuniform shear from this misalignment results in a nonuniform fiber orientation. The effects of the secondary flows of the second type are not well established yet. We believe that the cross streams due to the turbulent anisotropy result in more local nonuniformities in CD and MD. This gives nonuniform fiber orientation in MD.

We can adjust the insert tubes at the tube bank to minimize the cross flow at the slice and to eliminate the problems associated with nonuniform fiber orientation. We have used this approach to evaluate the hydrodynamics of a commercial headbox. The objective was to optimize the influx for a more uniform fiber orientation. Computation provided the optimized influx profile. The location of the insert tubes achieved the same influx profile obtained computationally. During a shutdown period, adjustment of the insert tubes at the tube bank accordingly gave notable improvement in the fiber orientation even at low rush to drag ratios.

The only way to obtain the secondary flows of the second kind is by direct numerical simulation of the full Navier-Stokes equations. This is very time consuming, and it is not practical for engineering applications. We are extending this work to calibrate the parameters in a nonlinear $\kappa - \epsilon$ model for computation of the secondary flows of the second kind in irregular geometries.

In the next section we discuss a technique called High-Speed Digital Imaging which our group at IPST uses for quantitative evaluation of paper forming hydrodynamics. A brief mention of this technique has been made in §3, though no particular details have been given. The next section presents this technique in greater detail. This same technique is later used in §7 for a quantitative analysis of the forming jet delivered from four different commercial headboxes.

# 6 High-Speed Digital Imaging of Paper Forming

## 6.1 Introduction

It is often important to know the characteristics of the forming jet to evaluate the headbox performance or to examine the wet end as a potential source of defects in the sheet properties. In this section, we present a method for quantitative evaluation and comparison of the forming jet hydrodynamics in commercial machines. This method is useful for investigating and eliminating wet end problems or for routine quality control of the forming section hydrodynamics. Our interest in implementing this method is primarily to investigate the source of the nonuniformities in formation, the methods to improve formation, and the result of any modifications on the formation characteristics. Visual inspection of the forming section has been a useful tool for many years in various studies of paper and board forming [10,47–50]. The ability to see the often important details in the forming layer depends on the visualization method. Simple inspection with the naked eye could reveal large and dynamically slow features of the flow. Frozen images using strobe lights or short exposure time photography (16 mm or 30 mm silver halide films) or videography (short exposure at 30 frames per second) are useful to some degree; however, many important details occur in fraction of a second and cannot be captured in slow framing rate visualization. High–speed digital imaging(1000 frames per second or greater) can reveal new phenomena, opening the door to significant improvements in the forming process. These images are recorded on an optical disk in digital form allowing computational analysis of the images. In this section, we describe a method for quantitative analysis of the forming section using high-speed digital imaging and image processing. This technique is used in the next section for evaluating the forming jets delivered from four commercial headboxes.

## 6.2 The Imaging Hardware Systems

The imaging system used in this study consists of a transportable Kodak Ektapro Motion Analyzer, Model 1000 HRC and a desktop Silicon Graphics workstation. The Kodak camera system is capable of collecting 1000 to 4000 images per second. The images are then archived to optical disk for later analysis. Archives of 500 images series (0.5 sec) with exposure times

of 0.06 msec are typical for this study. Each image is 512 pixels wide by 384 pixels high. One byte per pixel is used to digitize a gray level. This corresponds to 256 gray tones possible per pixel. The sensor uses CCD technology to expose the image. In this particular sensor, 16 CCD's are used to collect the image information. The image is divided into sixteen 64 by 192-pixel sections each employing a single CCD sensor. The pixel data are combined with a 1024-byte footer containing framing information to produce an image file of 197,632 bytes. A typical 500-image acquisition will require 94 megabytes of disk space.

## 6.3 Preparation of the Raw Images

The quality of the raw images acquired at the mill is limited due to poor lighting and limited access to the imaged area. We have developed methods to overcome these limitations and to considerably enhance the raw images for more effective analysis. After images are acquired, downloaded to optical disk, and transferred to a Silicon Graphics workstation they are ready for processing. We have written special software for various computational analyses of these image sets. All raw images are first patch equalized. Patch equalization is an image processing procedure based on histogram equalization. Histogram equalization is used to maximize the contrast (range) of each pixel in the raw image, however, it is not effective in balancing any uneven illumination. Patch equalization is an extension of histogram equalization that we have developed specifically to maximize contrast and to balance spot lighting.

At a mill, powerful halogen lights are used to illuminate the scene to a point where 0.06-msec exposures becomes possible. Even with a good on site lighting system, images will have bright areas and as a result the camera system will not take advantage of the full 8-bit grayscale. The standard technique in commercial image analysis programs to stretch an image over the full 8-bit range in histrogram equalization. However, histogram will not balance uneven lighting conditions. To counter spot lighting we have developed methods where the image is divided up into many patches. Each of these patches is histogram equalized. This will balance uneven lighting, however, the seams between patches become a visible artifact. To solve this problem, a moving patch is developed which is centered on the

current pixel. A neighborhood of pixels around the current pixel is used to form the local histogram for the equalization. Accumulation of histograms and equalization procedures for each pixel of an image in a 500-image set can become a computationally time-consuming effort. To accelerate the process, the requirement to accumulate histograms for each pixel is relaxed and the same histogram is used over small groups of pixels ($4 \times 4$ is typical). Since the patch over which the histogram is gathered is larger than the group it is applied to, seams at the patch boundaries are effectively equalized and the algorithm time is reduced significantly.

The patch and window sizes that display effective corrections are found to be $4 \times 4$ patch sizes with a $25 \times 25$ pixel floating window. Comparisons of the different histogram equalization methods are found in **Fig. 35**. A slight hallowing artifact may be introduced due to patch equalization under certain conditions. This can sometimes be seen on image edges and around sharp transitions to large constant features, such as headbox faces and large sharp shadows. These static features, if present, are of scales much larger than the dynamic features of interest and, as such, do not influence the final results.

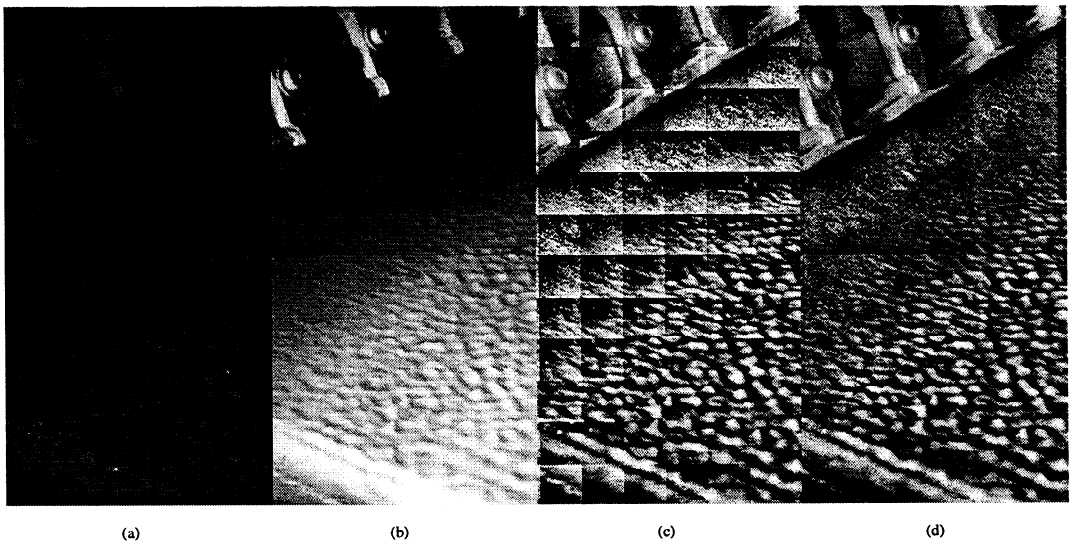


Figure 35: Comparison of Equalization Techniques, (a) Original Raw Image, (b) Standard Histogram Equalization, (c) Fixed Window Patch Equalization, (d)Moving Window Patch Equalization

## 6.4 Averaging and Time Series Image Processing

Once the raw series of images have passed through the patch-equalization stage they may be examined in detail. Two basic operations are performed to reduce the data. The first type of operation is averaging. The second type of operation is time series compilation.

The flow in the headbox and on a significant part of the forming section is turbulent. Turbulent flow is characterized by presence of flow fluctuations in time around a mean flow. The mean flow can be unsteady, however, the time scale for the mean flow is much larger than the time scale for the turbulent fluctuations. The mean flow is deterministic and predictable whereas the turbulent fluctuations have random characteristics. Given *"enough"* computational resources, the Navier–Stokes equations can be solved using direct computational methods for the turbulent velocity and pressure. However, except for very simple turbulent flows, today's computational resources are not adequate for direct turbulent analysis using the Navier–Stokes equtions. The more practical approach is to solve for the mean velocity and pressure, defined by

$$\bar{u}_i = \frac{1}{T}\int_t^{+T} u_i dt \quad \text{and} \quad \bar{p} = \frac{1}{T}\int_t^{+T} p dt \quad i = 1, 2, \text{ and } 3 \tag{34}$$

where the bar over the variable $u_i$ and $p$ represents the mean velocity vector and pressure, respectively, and the fluctuating component is defined by $u_i' = u_i - \bar{u}_i$. This requires modeling the Reynolds Stress term $\overline{u_i' u_j'}$, which arises in the mean N–S equations. In many cases, visualization of the mean flow becomes very important for understanding the flow characteristics. We have developed methods for construction of the mean flow pattern from the high-speed digital images of the turbulent flow in the forming section. In this process each pixel is accumulated for the entire image set and then divided by the total number of images. This operation removes electrical noise and random turbulent components. What remains is the mean flow field. Typically, 10, 50, 100, and 500-image sets are used to construct the mean flow. Once the average is produced it is patch-equalized to rescale the range of an 8-bit pixel range.

*Time series* compilation is used to record activity that passed a particular point over the acquisition time. The best way to illustrate this procedure is with an analogy. A room has

were not accurately measured.

The dynamics of the streaks on the forming table have been captured using a digital video system. Off-line image processing analysis and signal processing analysis and signal analysis techniques were employed to quantify the scale and regularity of the streaks, as outlined by Aidun and Ferrier [11] and in **Appendix B**. To facilitate the comparison of one paper-making machine to another, the data are plotted with similar scales and the image data are printed with overlaid grids. FFTs for the averaged images and the time- series images are presented and discussed. Furthermore, the FFT data may be directly compared across machines by plotting the ratio of standard deviation to the average value.

## 7.2 Results and Analysis

In the imaging of the forming jet and the forming layer, we have focussed on the fluid mechanics after the impingement line region. Despite our attempts, in some cases we were unable to access and record the images at the same relative distance from the slice and the impingement line. This is due to the differences in the headbox slice design and the location of the catwalk on the forming table. For the sake of accurate documentation, we have made careful records of the exact location on the forming table that has been imaged. Figures 37 and 38 show the typical overhead view layout and a map of the locations where each machine has been imaged. The distance from the imaging region to the slice has been outlined in Figure 38.

## 6.5 Spectral Analysis

The goal of the study is to examine and characterize nonuniformities on the table. At this point, we have the high-speed image data in a form that can meet this goal. Fourier methods are utilized to measure dominant wavelengths in the CD direction. The two types of reduced images formed display the streak features but in different ways. The averaged view removes any turbulent fluctuations and electronic noise leaving mean features, while the time series images retain the turbulent fluctuations and any electronic noise but show feature dynamics over time. Any one scanline in the CD direction may be passed through a Fast Fourier Transform (FFT) to recover any dominant wavelengths that make up these streak features. The frequencies of features across image may be correlated to physical parameters.

The FFT is a powerful statistical tool and much has been written on its use. An FFT of any signal can contain useful informaion about that signal, however, with some signal preconditioning misinterpretation of signal results can be reduced. In this study, signal amplitudes are de-trended and then windowed using a Hann function. For a full discussion of FFT methods the reader is referred to Bloomfield [51] or Press *et al.* [52]. Typical ranges of frequencies resolvable are 1/(2 pixels) to 1/(512 pixels). The relative distance the sensor positioned above the wire will determine the length scale within the image, however, 75 pixel/in. is typical. This scale results in frequencies of 38 cycles/in. to 0.2 cycle/in. No aliasing of harmonics has been seen as most of the information is typically below 5 cycles/in., well below the highest frequencies resolvable [51].

## 6.6 Evaluation of Time Series Images Using FFT Methods

The raw data have been patch equalized and recomposed into two different forms: *averaged images and time series images.* The time series images were analyzed using FFT methods and will be discussed here. Averaged images will be discussed in the next subsection. To begin, a typical CD scanline was chosen and an FFT was made of this scanline. Since the time series data contain turbulent information, a single scanline may not show a frequency of a large scale streak. To examine the range of turbulent frequencies and expose any non-

turbulent effects an FFT was taken, accumulated, and averaged. This exposes dominant frequencies and shows that turbulent frequencies cover a continuous range.

## 6.7 Evaluation of Averaged Images Using FFT Methods

The average images were also analyzed using FFT methods. Similarly, a typical CD scanline was chosen and an FFT was made of this scanline. However, since the time series data contain little turbulent information, a single scanline in this case distinctively shows frequencies of any large-scale streaks. The averaged overhead views often display the evolution of mean features down the viewed portion of the table; it is useful then to examine the change in the FFT for each CD scanline down the table. The top 4 peaks are recorded for the FFT of each scanline and plotted against scanline number (position down the table). Any shift in dominant frequencies down the table can be illustrated. Similarly, if the magnitudes of the major peaks are recorded then the relative significance of the peaks can be seen. In this way the continuity of the streaks down the table can be illustrated.

To find the peaks of an FFT and to rank them by magnitude, the following algorithm was developed. First, an array of zeros is created such that the length of the array is the same as the number of points in the FFT. This is the 'accountant' array. The maximum and minimum values of the FFT are found. Second, the value of the maximum is replaced with the value of the minimum such that it will not be found again. At the position of the last found maximum, a 1 is recorded in the accountant array. The position in the accountant array is examined. If this position has no 1's as immediate neighbors, then its magnitude and value are recorded. Third, the next maximum is found and the process continued until the required number of ranked peaks are recorded or the next found maximum equals the minimum. The recorded peaks will be ordered from highest to lowest magnitude.

## 6.8 Conclusions

Much can be learnt by digital imaging of the forming section and subsequent analysis and manipulation of the images. The raw images can be enhanced to better capture the details of the forming jet, the jet impingement, and the forming layer dynamics along the forming

table. Spectral analysis of the images and timeline imaging can be used to evaluate the performance of the headbox and the quality of the forming jet. In fact, detailed imaging can be used to obtain a qualitative level of surface turbulence (RMS) in the forming jet, in addition to the mean flow structure. Even though here we have concentrated on light reflection from the surface of the forming jet, the same approach can be used for light transmission imaging through the forming to evaluate the uniformity of fiber dispersion and the degree and rate of floc formation on the forming table.

In the next section, we use this high-speed digital imaging technique to quantitatively evaluate the forming jets from four different commercial headboxes.

# 7 Quantitative Evaluation of the Forming Jet Delivered from Four Different Headboxes

## 7.1 Operational Parameters of Four Hydraulic Headboxes

Considering that there are a variety of headbox and forming sections, we selected four machines which cover the different design features that are most popular in commercial headboxes. Also, we have chosen two of the headboxes to have similar designs for comparison of the imaging method. These machines all have Fourdrinier forming sections with relatively easy access for side and top views. During the imaging studies, these commercial machines were operating under slightly different parameters, but all producing base sheet coated paper. The four Fourdrinier paper machines considered in this study operate under somewhat similar conditions, although being commercial, the operating parameters are not exactly the same. **Table 3** summarizes these parameters. Note that all of the data have been provided by the mill.

Table 3: **List of parameters for the four paper machines**

| Machine | Machine Width (in.) | Headbox Flow Rate (gpm) | Wire Speed (fpm) | Rush Drag | Consistency | Slice Opening (in.) |
|---|---|---|---|---|---|---|
| A | 332 | 18,922 | 2917 | 0.997 | 0.61 | 0.45(2) |
| B | 234 | (1) | 2640 | 0.992 | 0.65 | 0.55(2) |
| C | 265 | 17,808 | 3000 | (3) | 0.90 | 0.55(4) |
| D | 302(5) | (6) | (1) | 1.005(8) | (9) | 0.49(10) |

**Notes:**
(1) not reported
(2) These values may not be very accurate($\pm 10\%$)
(3) not reported
(4) given as: $vert. = 0.55''$, $hori. = -0.46''$
(5) given as: $wire = 302''$, $slice = 294''$, $reel = 272''$
(6) range given as: 16,000 – 24,000
(7) range given as: 2,000 – 3,4000
(8) given as: $J/W = 1.005$
(9) range given as: 0.40 – 0.75
(10) range given as: $0.4'' - 0.6''$; typical values listed in the table.

Some of the parameters are given as a range within an estimate of the operating value. In these cases, the note below the table specifies the range. Some parameters given by the mill

were not accurately measured.

The dynamics of the streaks on the forming table have been captured using a digital video system. Off-line image processing analysis and signal processing analysis and signal analysis techniques were employed to quantify the scale and regularity of the streaks, as outlined by Aidun and Ferrier [11] and in **Appendix B**. To facilitate the comparison of one paper-making machine to another, the data are plotted with similar scales and the image data are printed with overlaid grids. FFTs for the averaged images and the time- series images are presented and discussed. Furthermore, the FFT data may be directly compared across machines by plotting the ratio of standard deviation to the average value.

## 7.2 Results and Analysis

In the imaging of the forming jet and the forming layer, we have focussed on the fluid mechanics after the impingement line region. Despite our attempts, in some cases we were unable to access and record the images at the same relative distance from the slice and the impingement line. This is due to the differences in the headbox slice design and the location of the catwalk on the forming table. For the sake of accurate documentation, we have made careful records of the exact location on the forming table that has been imaged. Figures 37 and 38 show the typical overhead view layout and a map of the locations where each machine has been imaged. The distance from the imaging region to the slice has been outlined in Figure 38.

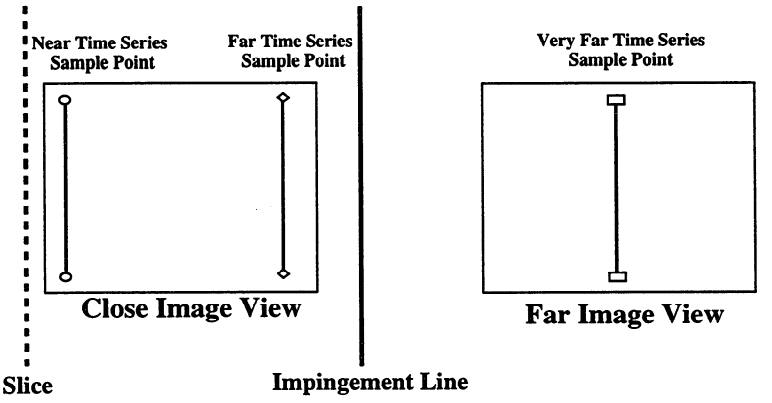


Figure 37: Typical overhead view layout showing image positions and time series sample points

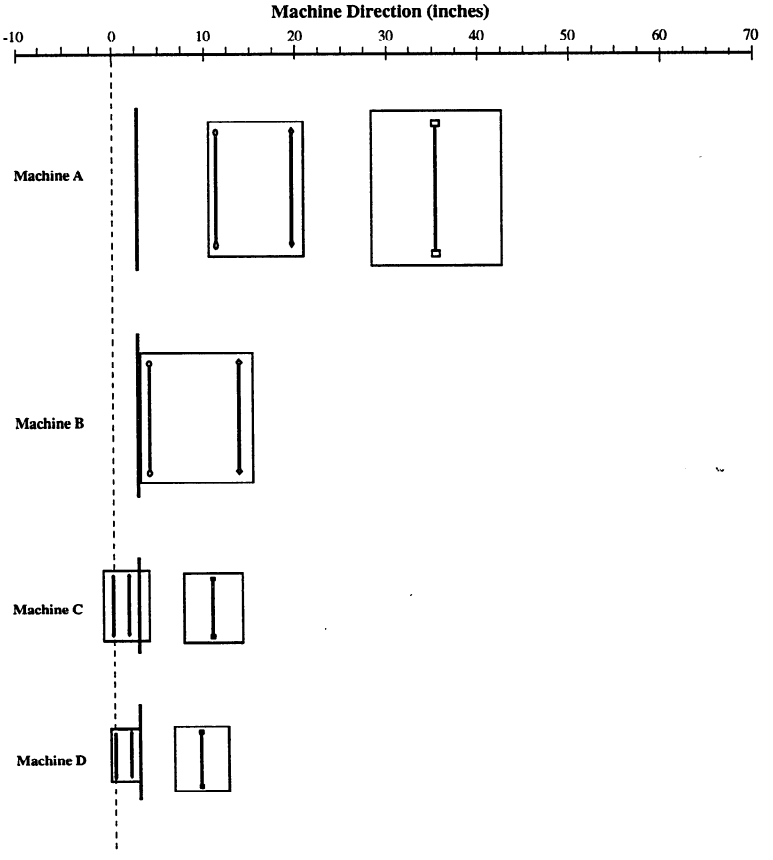


Figure 38: The locations imaged for each machine

The range of the forming table covered in the imaging study and the position of the samples are outlined in **Tables 4** and **5**. For machines A and B we were unable to image the forming jet before the impingement line. Therefore, in the comparison of the images, we focus on the region after the impingement line for all cases.

Table 4: **Averaged Images – Range of Table Covered**

| Machine | Start of Close Image (in. from slice) | End of Close Image (in. from slice) | Start of Far Image (in. from slice) | End of Far Image (in. from slice) |
|---|---|---|---|---|
| A | 11.5 | 23.4 | 28.8 | 42.3 |
| B | 4.0 | 21.5 | - | - |
| C | -1.1 | 6.1 | 13.0 | 20.1 |
| D | 0.0 | 5.0 | 9.0 | 17.4 |

Table 5: **Time Series Images – Positions of Samples**

| Machine | Near (in. from slice) | Far (in. from slice) | Very Far (in. from slice) | Impingement Line (in. from slice) |
|---|---|---|---|---|
| A | 12.8 | 20.9 | 35.5 | 4.0 |
| B | 7.0 | 15.5 | - | 4.0 |
| C | 0.5 | 3.5 | 16.5 | 4.8 |
| D | 0.5 | 4.5 | 13.5 | 5.5 |

Typical enhanced images of the forming jet are shown in **Figs. 39a-d** for machines A to D, respectively. These images are taken at 0.06-millisecond exposure time at 1000 images per second. The forming jet is illuminated by 1000 W Tungsten light from the side of the forming table. The streaks in the forming jet reflect the incident light at varying intensites to the camera depending on the nonuniform curvature of the liquid surface. In principle, from these images, one can calculate the amplitude of the streaks or waves from the intensity of the recorded light. However, this approach requires a more precise control on the light intensity, a requirement not easily achieved in the mill during a commercial run without interference with the operation and production of the machine.

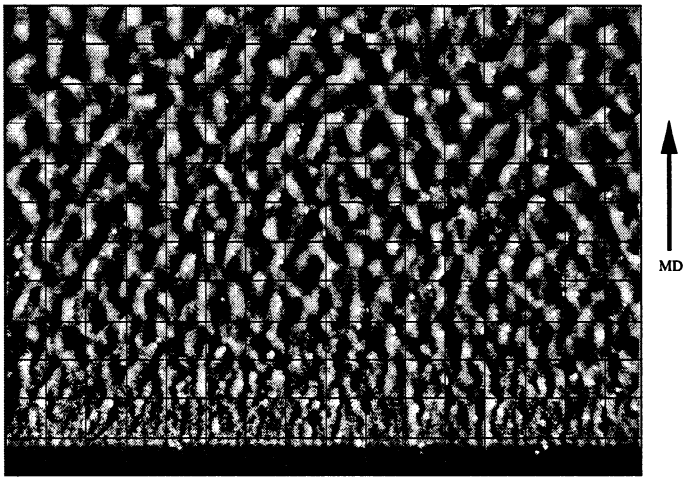


Figure 39: (a) Single frame image of the forming jet after impingement on the forming wire of machine A. The gridlines show a 1-inch length scale

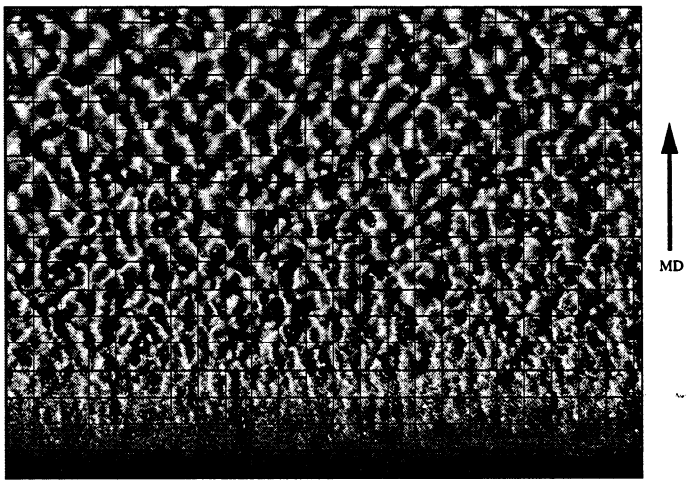


Figure 39: (b) Single frame image of the forming jet after impingement on the forming wire of machine B. The gridlines show a 1-inch length scale

Visual inspection of the images in Figures 39(a–d) provides some view of the forming jet characteristics. One can immediately see slight nonuniformities in CD as well as MD with more or less in all of the forming layers. Jet roughness and small structures in the forming jet result from turbulent flow inside the headbox as well as the mean secondary flows. The scale of the surface roughness seen on the forming layer in Figures 39(a-d) is related to the

turbulent eddy size and strength. There are some similarities between images for machines A and B. Also, machines C and D, having very similar features show similar forming layer patterns after the impingement line. The impingement angles in these machines are different, therefore, the degree of stock jump after impingement would be different. However, we are more concerned about the surface pattern and regularity of flow on the forming table.

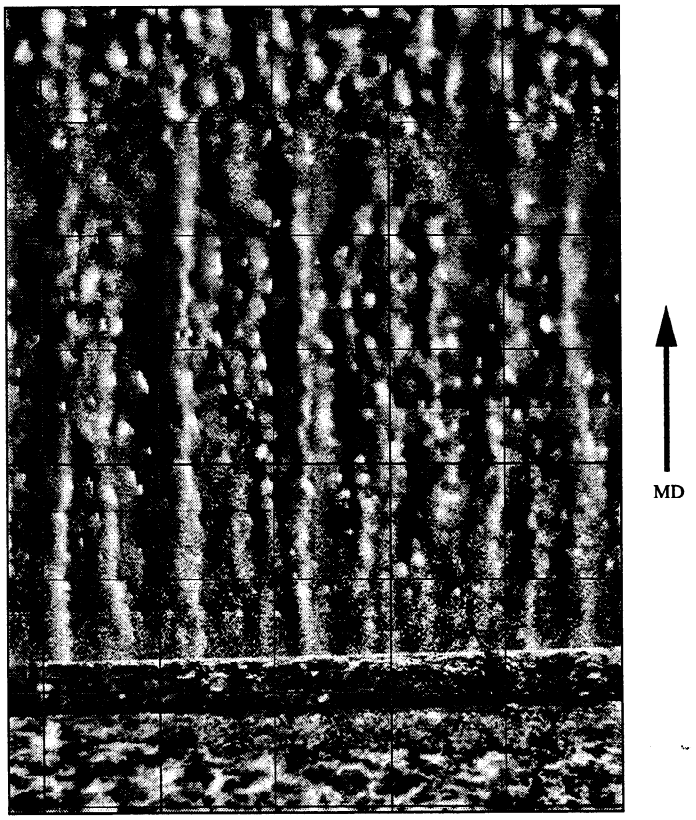


Figure 39: (c) Single frame image of the forming jet after impingement on the forming wire of machine C. The gridlines show a 1-inch length scale

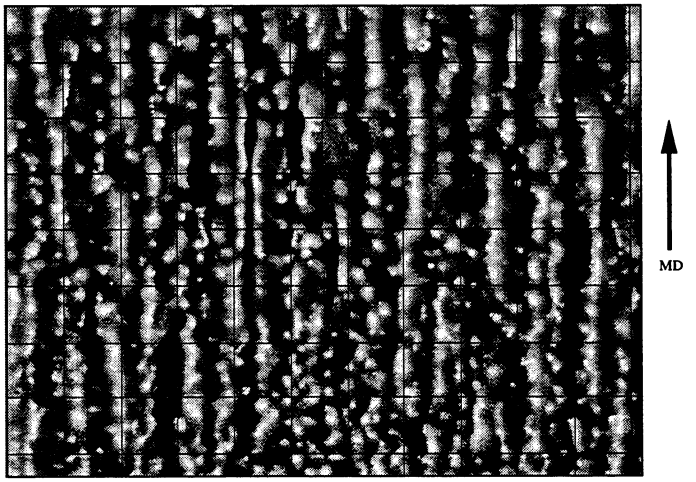


Figure 39: (d) Single frame image of the forming jet after impingement on the forming wire of machine D. The gridlines show a 1-inch length scale

Comparison of the A and B forming layers, shown in Figures 39(a and b), with C and D forming layers, shown in Figures 39(c and d) reveals a fundamental difference in the pattern. The A and B layers show jagged streaky pattern where C and D layers show a relatively straight streak in the machine direction. The reason for this difference, we believe, is a fundamental difference between the A & B headboxes and those on machines C & D. The headbox on machine A has one set of tube bank, the tube column is inclined, and there are vanes or sheets in between the rows of tubes. Headbox B also has one tube bank with a regular vertical column and vanes or sheets between the tube rows. Machines C and D have almost identical headboxes. These headboxes have a set of manifold tubes, a 'stilling chamber' and 3 rows of staggered tubes in the second bank of tubes prior to the converging nozzle. There are no vanes or sheets inside the converging nozzle of the C and D headboxes.

As we have outlined elsewhere [10], the interaction of the jets from the tubes inside the headbox generates mean secondary flows which result in a regular streaky pattern on the forming table. The jets from the tubes are squeezed onto neighboring jets, below and above, generating mean secondary flows in the form of counter-rotating vortices. With headboxes A and B, the sheets delay the interaction of the jets in this manner.

We take the average of the flow over 0.1 sec. (i.e., 100 frames) and present the results in Figures 40(a–d) for machines A – D, respectively. We see deterministic streak patterns in

all the cases, although case B shows much noise (random variations) in the averaged image. The grid lines superimposed on the images represent a 1-in. length scale. To evaluate the degree of regularity of the streaks, we cannot rely on the visual inspection of these images or the averaged images. For a quantitative method of evaluation, we compute the average and the standard deviation of the FFT of each CD scanline of the image averaged over 100 frames (i.e., the image presented in Figures 40(a-c) for each machine, and averaged over 300 frames for Figure 40d).

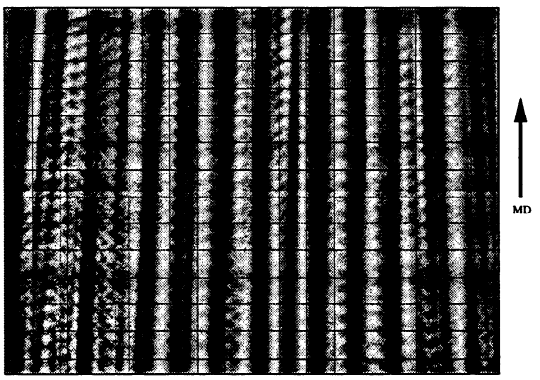


Figure 40: (a) Image averaged over 100 frames (0.1 sec) of the post-impingement forming layer on the forming wire of machine A. The gridlines show a 1-inch length scale

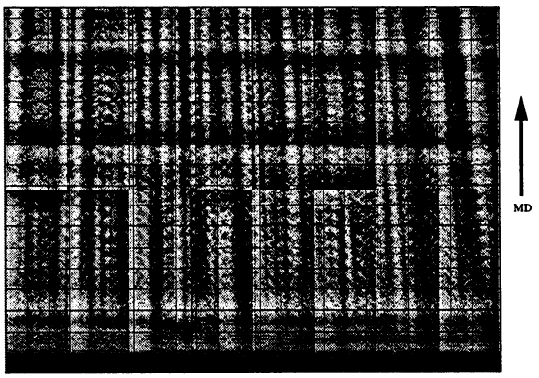


Figure 40: (b) Image averaged over 100 frames (0.1 sec) of the post-impingement forming layer on the forming wire of machine B. The gridlines show a 1-inch length scale

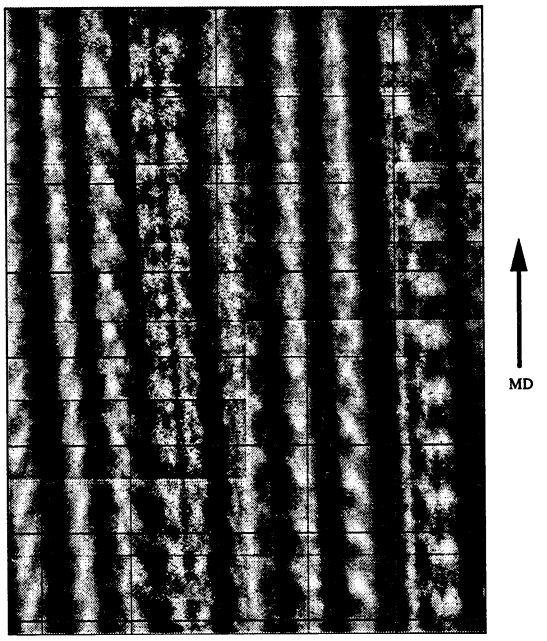


Figure 40: (c) Image averaged over 100 frames (0.1 sec) of the post-impingement forming layer on the forming wire of machine C. The gridlines show a 1-inch length scale

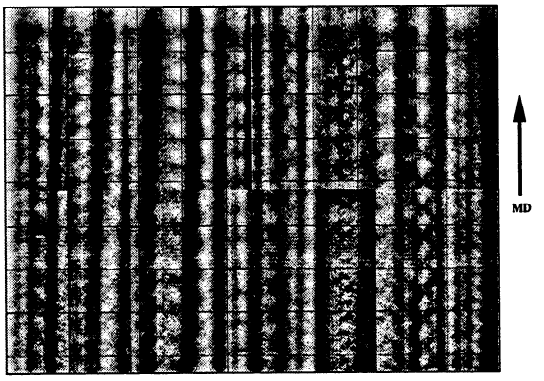


Figure 40: (d) Image averaged over 100 frames (0.1 sec) of the post-impingement forming layer on the forming wire of machine D. The gridlines show a 1-inch length scale

The more regular and persistent the streaks are, the smaller the standard deviation of the FFT divided by the mean value of the FFT will be. For a rigorous evaluation, we need to make the comparison at equal headbox and forming section parameters: that is, equal slice opening, machine speed, average jet velocity, jet impingement angle, and the ratio of

the average jet velocity to the wire speed. However, we could not find two machines that operated with exactly the same values of these parameters. the four machines considered in this study were the closest we could get to the ideal case.

With the understanding that the difference in the operational parameters, as listed in **Table 3**, between these machines could influence the quantitative results, we present the comparison of the FFT standard deviation/averaged FFT for 100 and 500 frames (i.e., 0.1 and 0.5 sec) in Figures 41 and 42, respectively. We have included the 500-frame averaged FFT result to demonstrate that the number of frames considered in this evaluation, as long as at least 100 frames are considered, does not change the conclusions. The frequency range of interest is between $0.5 - 2$ in.$^{-1}$, that is 2 to 0.5 in. length scale. The dominant streaks in machines C and D are in the range of 0.5 to 1 in. length scale, where for machines A and B, the dominant length scale is 1 to 2-in. In the 0.5 to 2 in. range, the standard deviation of machines C and D are lower than the standard deviation of images taken from machines A and B. This shows more regularity in streaks for machines C and D.

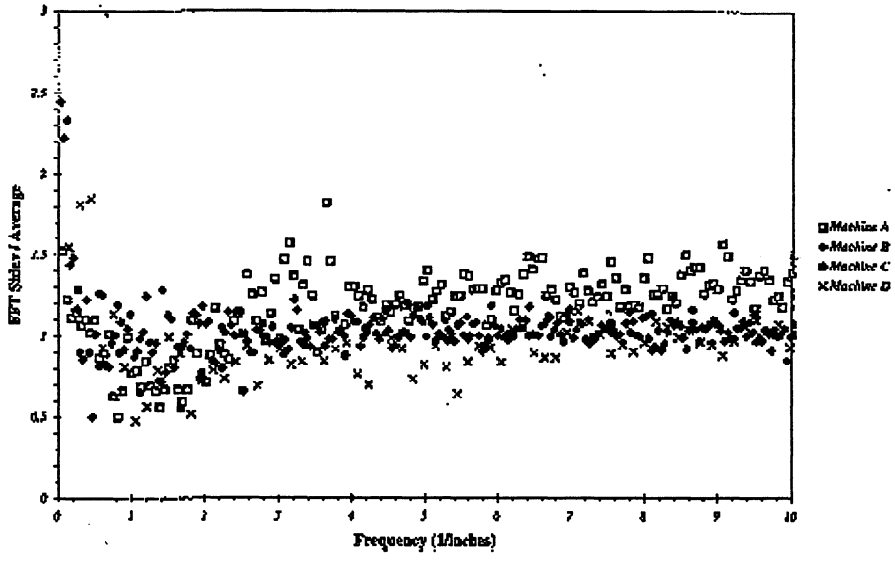


Figure 41: The FFT standard deviation/average for all scanlines after the jet impingement line – 100 frames

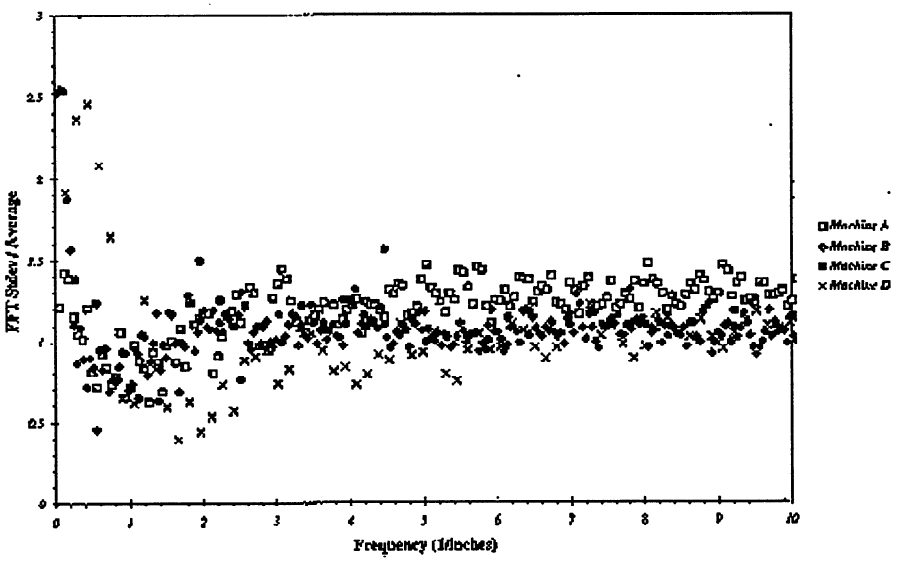


Figure 42: The FFT standard deviation/average for all scanlines after the jet impingement line – 500 frames

In general, the results show that the images of the streaks for machines A and B are less regular than the streaks generated in machines C and D about the 1-in. length scale. About the 2-in. length scale, machines C and D show the most regular streak pattern. This method of comparison does not make an evaluation of the amplitude of the streaks; it is just the persistence or regularity of the streaks that is measured. The amplitude of the streaks is strongly influenced by the jet impingement angle and the jet velocity.

The question is why do headboxes A and B, in general, deliver jets with less regular streaks than headboxes C and D in the 0.5 to 1-in. range. Although we have not rigorously analyzed the difference between these headboxes, some ideas can be considered. The main difference between the converging nozzle of these headboxes is that both A and B have sheets extending from the tube outlet to a few inches from the slice separating the jets from each row of tubes, where headboxes C and D have no sheets. Therefore, the jets from adjacent rows in headboxes C and D can interact immediately starting from the outlet of the tubes. One may conjecture two mechanisms based on this difference in the converging nozzle geometry, as outlined below:

One, the sheets inside the headbox provide 'additional turbulence', as reported. The higher

turbulence level (we assume higher turbulence level referred to in the industry is higher value for turbulent kinetic energy defined as the trace of the Reynolds Stress Tensor) results in damping or flattening the velocity profile from the tube jets and provide a more random jet delivered from the slice. We doubt that this is the mechanism since our measurements of the turbulent kinetic energy in a headbox very similar to headbox A shows an increase in the turbulent kinetic energy (most likely due to an increase in the turbulent eddy scale) by removing the sheets from the headbox [see §5.1].

The second mechanism is based on isolating the jets from each row of tubes and therefore, preventing the interaction of the tube jets with their neighbors in the rows above and below. Computational analysis of the flow in the converging zone of the nozzle shows that as the jets from two rows interact, a mean secondary flow of counter-rotating vortices form for each pair of jets [10,11]. These vortices generate streaks at the slice and on the forming table. When a solid surface isolates the rows of jets, the early interaction of the jets with the adjacent jets from the rows above and below are delayed until further downstream in the converging nozzle. This changes the mechanism of interaction among adjacent jets and, therefore, alters the pattern of the streaks on the forming table. The relatively straight streaks are replaced with considerably jagged streaks. However, the jagged streaks are still formed along the machine direction, as the averaged image in Figures 40(a and b) show. At this time, the exact mechanism for the formation of streaks in headboxes with vanes is not clear to the author. We are now engaged in detailed computational analysis of a headbox with sheets in the converging zone. The results which will appear in future publications would provide some insight into the fluid mechanics of the forming jet by this class of headboxes.

To further investigate the characteristics of the forming jet from the four headboxes considered in this study, let us analyze the timeline images of the forming sections as presented in Figures 43(a–d) for machines A to D, respectively. An explanation of the timeline imaging has been given in §6 and **Appendix B.**

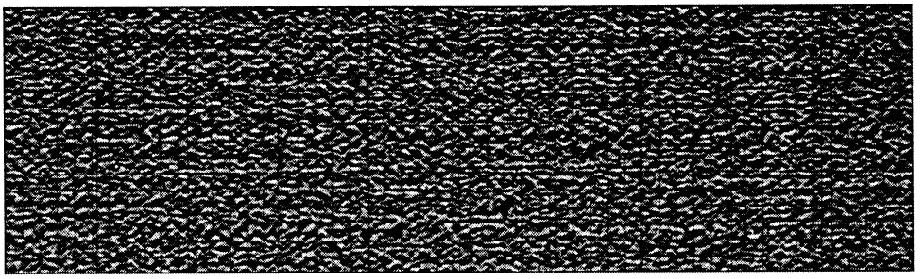


Figure 43: (a) 100-ms time-series image of the forming section of machine A at 15″ from the slice. The blue gridline shows a 1-inch length scale and the sections bounded by the red lines represent a 100ms increment

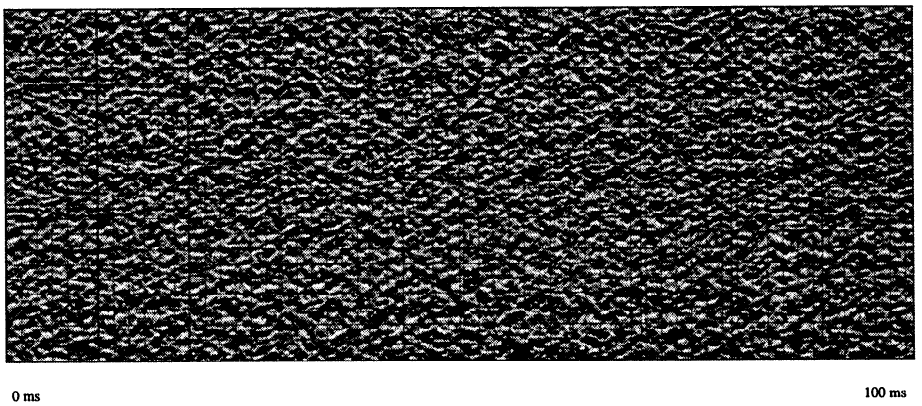


Figure 43: (b) 100-ms time series image of the forming section of machine B at 15″ from the slice. The blue gridline shows a 1-inch length scale and the sections bounded by the red lines represent a 100ms increment


Figure 43: (c) 100-ms time-series image of the forming section of machine C at 15″ from the slice. The blue gridline shows a 1-inch length scale and the sections bounded by the red lines represent a 100ms increment

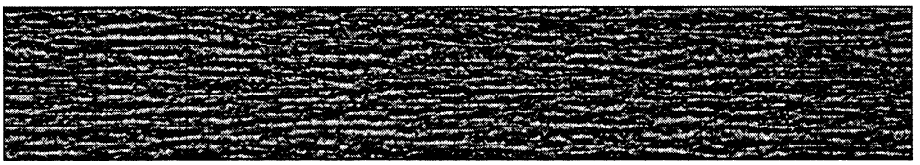


Figure 43: (d) 100-ms time-series image of the forming section of machine D at 15″ from the slice. The blue gridline shows a 1-inch length scale and the sections bounded by the red lines represent a 100ms increment

These images show the dynamics of the flow pattern in the forming jet. The images are taken at a section of the forming jet about 15 inches away from the slice. The impingement line in all cases is about 4 to 6 inches from the slice. Machines A and B, in general, show a different surface flow pattern than machines C and D. The streaks in machines C and D are more elongated in the machine direction. We hesitate to make any conclusions from visual inspection of these images.

In general, one assumes that the smaller scale eddies in the forming layer provide a more effective mechanism for preventing fiber flocculation. Some previous studies have addressed this issue [48-50].

In the next section we study an experimental headbox to understand the mechanism of turbulence in CD, MD, and ZD.

# 8 Investigations of Experimental Headboxes

## 8.1 Effect of Contraction Ratio on Fiber Orientation

Headbox guide sheets and headbox contraction ratio are among the structural parameters that greatly influence the orientation of fibers in the finished paper. This has been demonstrated by Mats Ullmar and Bo Norman [15]. Contraction Ratio (CR), as defined by them, is the ratio of headbox nozzle inlet area to nozzle outlet area. They constructed experimental equipment to study the fiber orientation in a headbox nozzle by mounting a CCD camera over the outlet together with a stroboscope. Image analysis has been used to evaluate fiber orientation from the recorded images. The fibers used in this investigation were polymer fibers of mean length and diameter of 3 mm and 45 $\mu$m, respectively. Experiments have been conducted for different contraction ratios by altering the slice opening at the nozzle end. They also conducted experiments for various flow velocities for each of these contraction ratios. Their results indicate that the effect of CR is more significant in fiber orientation than in flow velocity. The fibers have been found to be more strongly oriented in the machine direction for higher CR's. This is also supported by an earlier paper by the same group [22] which showed that an increase in the CR results in an increase of the MD/CD tensile stiffness ratio of the paper due to more fibers oriented in the MD.

## 8.2 Effects of Guide Sheets on Headbox Hydrodynamics

To complement the above study, we present the results of two sets of experiments done by our group in which we measured velocity profiles and turbulence intensities using LDV [53] (also see Appendix A) at the jet exit and in the headbox, with and without the guide sheets in place. Our results show that the guide sheets effectively reduce both the average cross-flow velocities and normal Reynolds stresses in CD, MD, and ZD, and provide more uniform velocity profiles than the headboxes without them. Both sets of experiments were done with and without the guide sheets in place. All measurements are at a flow rate of $50.5L/s \pm 3$ % (800 gpm) with a slice opening of 12.7 mm (0.5 in.). The headbox width is 406 mm (16 in.); so the average jet velocity at the exit is 9.8 m/s. The headloss in the headbox is somewhat higher with the sheets than without.

## 8.3 Measurements at the Jet Exit

Vertical profiles of the variation of the horizontal streamwise, $u$, and cross-flow velocity, $v$, at the jet exit were made at five horizontal locations as shown in Figure 44. The horizontal locations were at $y = 2,\ 4,\ 8,\ 12$, and 14 in. The vertical coordinate, $z$, of the point of measurement is the distance from the Lucite attached to the lower surface of the slice. The laser probe is placed below the Lucite looking upwards as shown in **Fig. 44**. Three measurements were recorded at each location. Data were obtained both with the separating plastic sheets inside the headbox and with them removed.

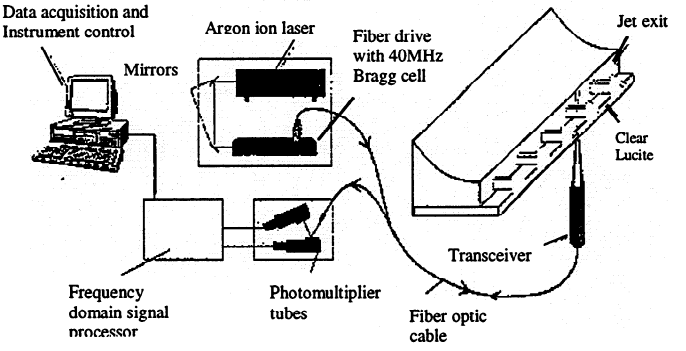


Figure 44: Schematic depiction of LDV experimental configuration

The mean streamwise and cross-flow velocities are shown in Figures 45 and 46. Typical streamwise velocities are greater than the average velocity at the jet exit due to the vena-contracta effect. It can be seen that the streamwise velocity is not exactly uniform. The variation of velocity over the cross section is about 3% of the mean value. Without the sheets, the variation is almost 10%. The results also imply some asymmetry of the flow about the jet exit centerline. The flow closer to the headbox inlet ($y = 14$ in.) is less uniform than farther away ($y = 2$ in.).

The cross-flow velocity is very small, essentially zero, with the sheets installed, implying essentially straight streamlines parallel to the headbox axis with negligible secondary circulations. The magnitudes are substantially higher without the sheets. For this case, the

velocities are generally negative to the left of the headbox centerline, and positive to the right. This implies diverging flow to the headbox walls. At the far wall ($y = 14$ in.) especially, the velocities are negative near the free surface and positive near the middle and lower boundary. This implies a rather strong secondary circulation within the jet, which is suppressed by the sheets.

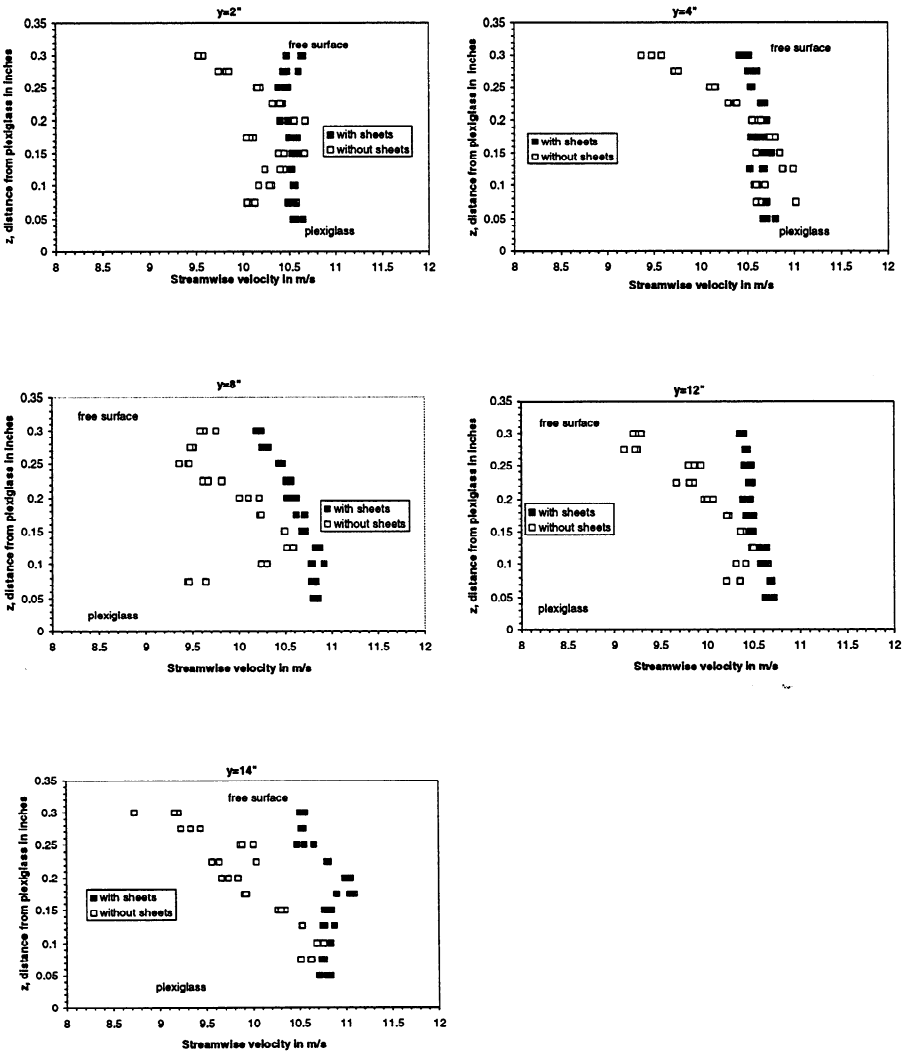


Figure 45: Mean streamwise velocity, u, at the jet exit with and without sheets

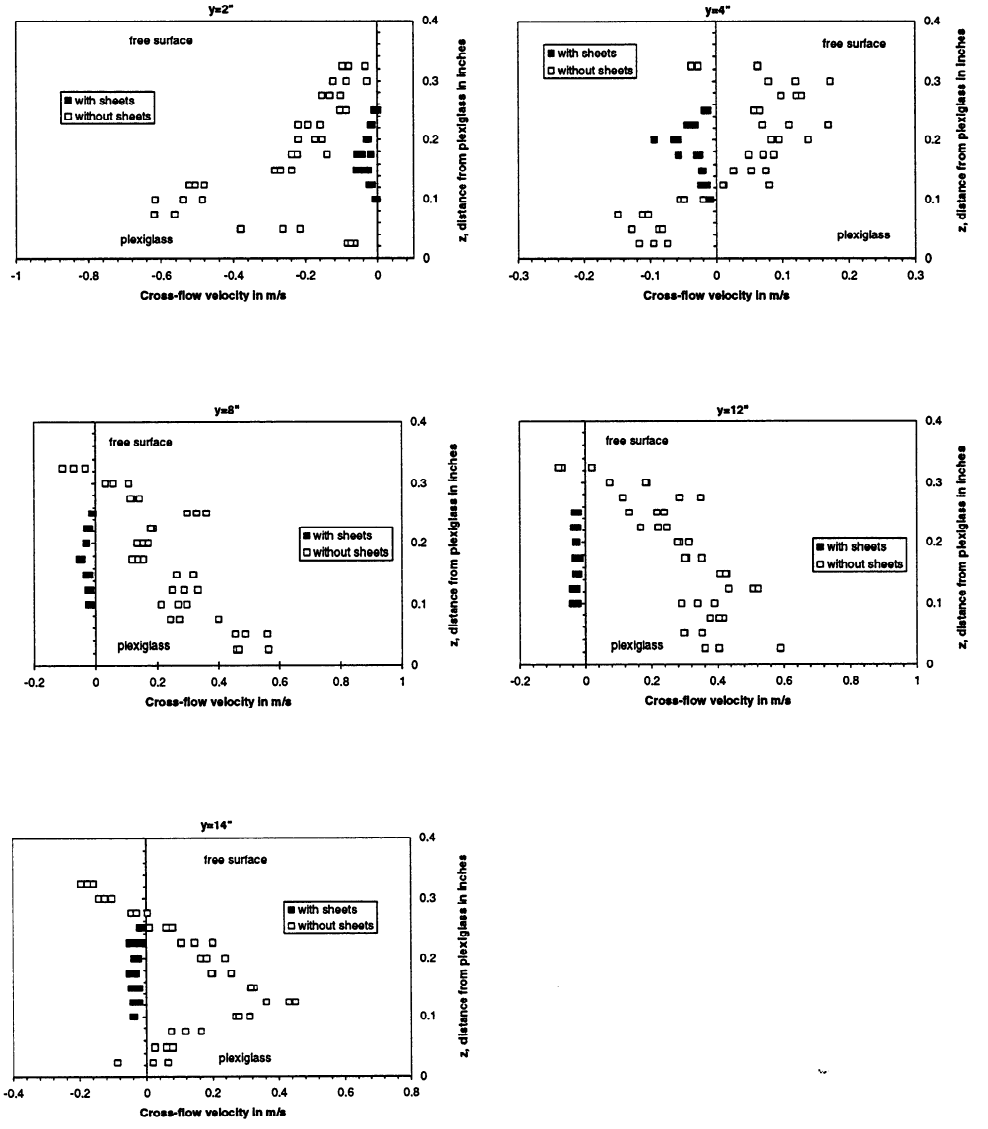


Figure 46: Mean crossflow velocity, v, at the jet exit, with and without sheets

The streamwise and crossflow variations of turbulence intensity (proportional to the normal Reynolds stresses) are shown in Figures 47 and 48. They are shown as the magnitude of the root mean square (rms) value of the velocity fluctuations from the local mean value.

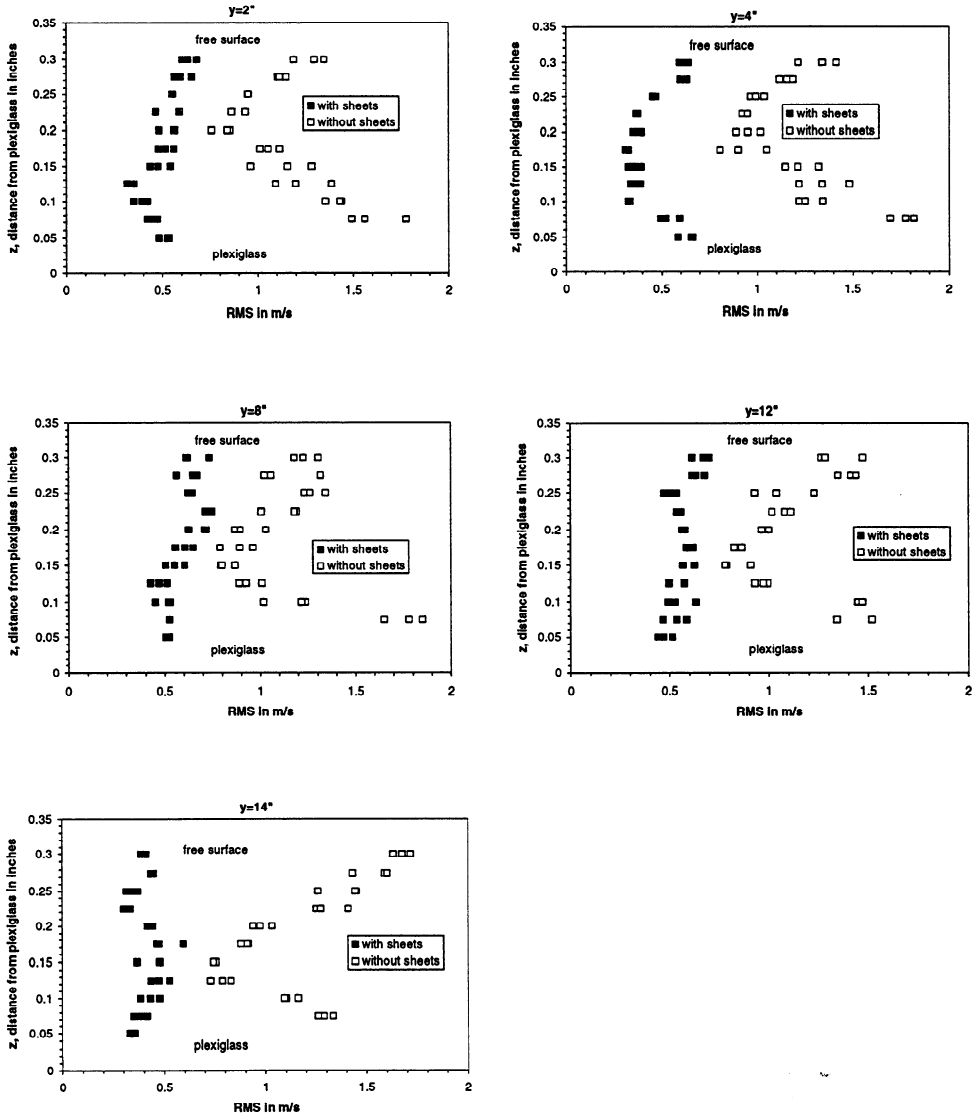


Figure 47: rms streamwise velocity, u′, at the jet exit, with and without sheets

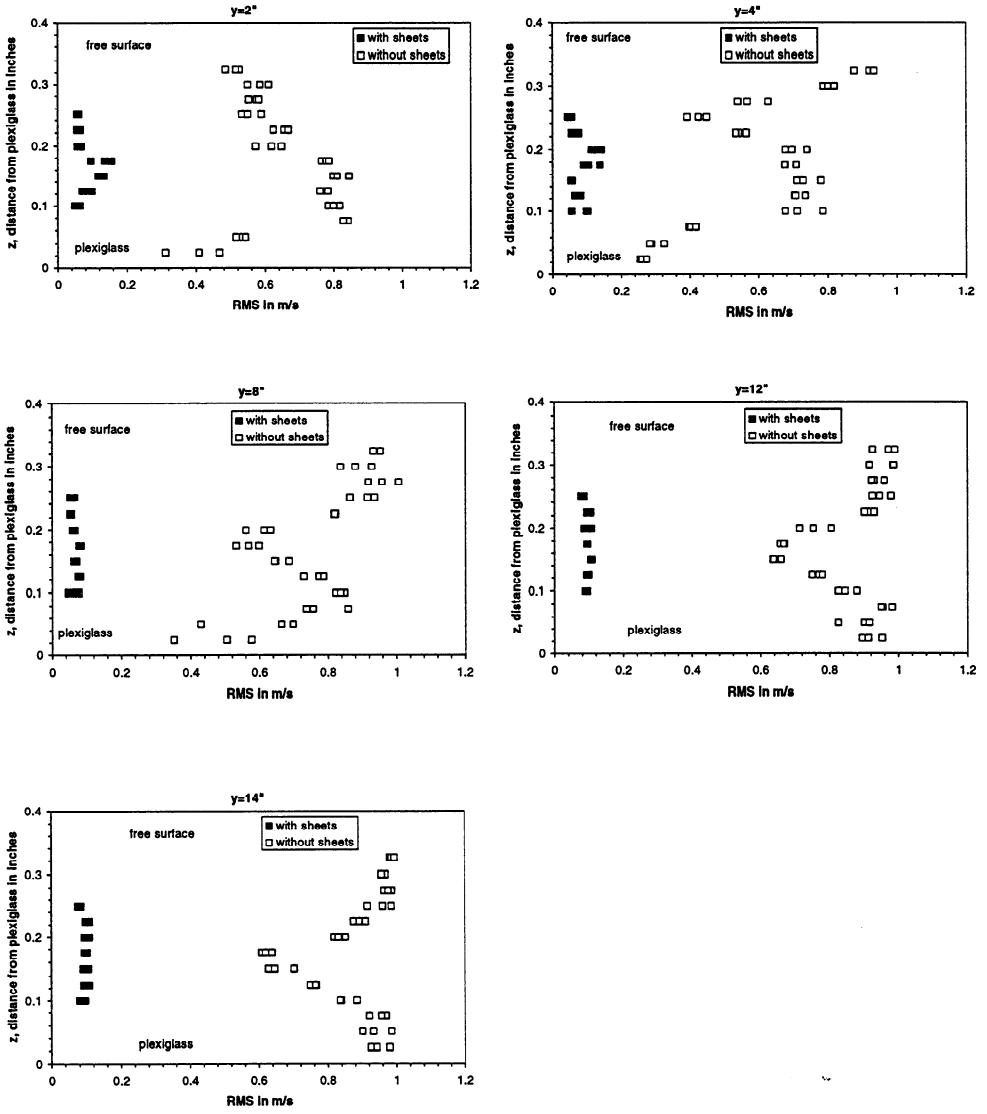


Figure 48: rms crossflow velocity, $v'$, at the jet exit, with and without sheets

The rms of the streamwise velocity is smaller and more uniform with the sheets than without. Typical streamwise values with the sheets are about $0.3 - 0.6$ m/s, corresponding to relative turbulence intensities of about $3 - 6\%$. The crosswise rms values are smaller, indicating that the turbulence is not isotropic. Without the sheets the rms values are higher and less uniform. Streamwise turbulence intensities are typically 10% greater and are higher near the lower boundary and at the free surface.

## 8.4 Measurements in the Headbox

Measurements of the streamwise velocity, $u$, and vertical velocity, $w$, were made inside the headbox along the longitudinal axis. The measurements were made at a distance $y = 3''$ from the Lucite wall along the centerline of the headbox. The longitudinal variations of the mean streamwise and vertical velocities and their rms values are shown in Figures 49 and 50 respectively.

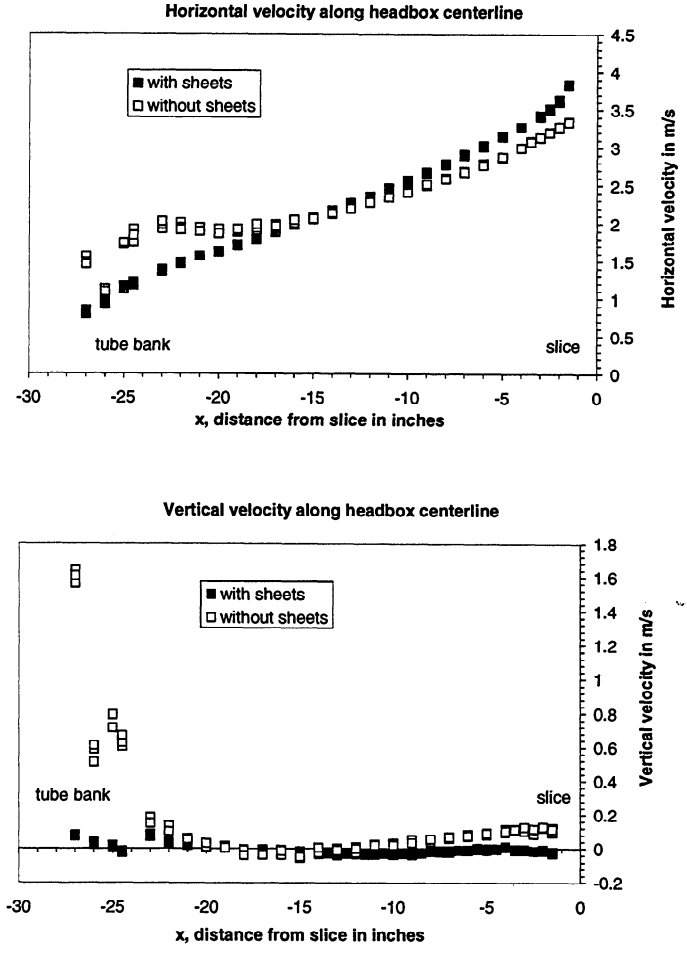


Figure 49: Mean streamwise velocity, u, and vertical velocity, v, along headbox centerline

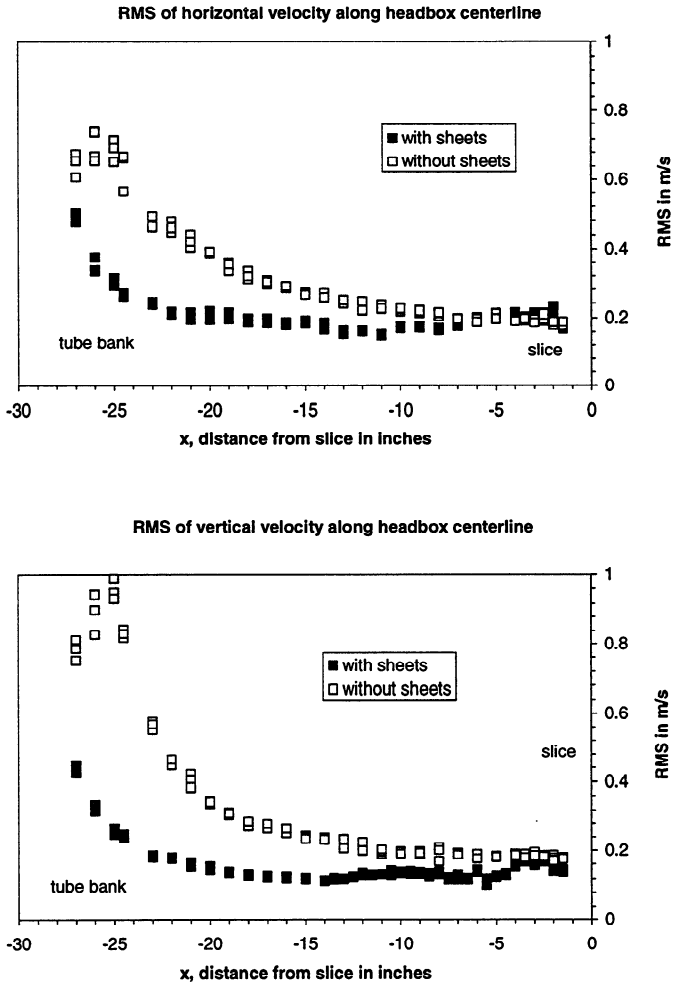


Figure 50: rms streamwise velocity, $u'$, and vertical velocity, $v'$, along headbox centerline

The streamwise velocity increases along the headbox due to the tapering cross section. Without the sheets, the streamwise velocity is larger near the tube and smaller near the slice than with the sheets. With the sheets, the velocity increases more uniformly along the headbox. The vertical velocities with the sheets are very small. Without the sheets, the vertical velocity is quite strong, up to about 1.8 m/s near the inlet tube bank. This velocity is positive, i.e, upwards. It is also positive near the jet exit but with a much smaller magnitude, about 0.1 m/s.

The streamwise rms intensities are smaller with the sheets installed than without them as shown in Figure 50. This is particularly true near to the inlet tube bank, where typical rms

values are about twice as large without the sheets. The difference decreases with distance along the headbox until the jet exit, where the rms values are very close. The relative turbulence decreases rapidly with distance along the headbox. With the sheets, it is from about 40% near the tube bank to about 3% near the jet exit. The high values near the inlet tubes are presumably due to the shear induced by individual jets issuing from the tubes. This turbulence decays with distance until by the jet exit it has been replaced by turbulence due to shear at the top and bottom boundaries of the headbox, with typical values around 3%.

## 8.5 Summary

1. The streamwise velocity of the flow leaving the headbox at the exit is more uniform with the sheets.

2. The cross-flow velocities are very small with the sheets. This indicates that secondary circulations are virtually eliminated by the sheets.

3. Cross-flow velocities without the sheets can be quite substantial and spatially variable. This indicates the presence of secondary circulations.

4. The magnitude of the turbulent fluctuations(expressed as their rms values) are smaller and more spatially uniform over the jet exit with the sheets than without. Relative turbulence intensities over the jet exit are typically about $3-6\%$ with the sheets and larger without.

5. The streamwise velocity inside the headbox increases more uniformly with the sheets than without them. Vertical velocities in the headbox are essentially eliminated by the sheets but can be quite large without them.

6. With the sheets, the relative turbulence intensity decreases rapidly with distance inside the headbox. It is about 40% near the inlet tubes and about 3% near the jet exit. This is presumably due to the decay of the turbulence intensity associated with the multiple inlet jets.

In the next section we examine five different types of tubes from various tube banks to study the effect of spiral fins, placed inside the tubes, on the average fluid velocities and turbulent intensities at their outlets.

# 9 Conclusions

Three of the major quality concerns in today's paper mills are the uniformity of basis weight, fiber network structure (formation) and fiber orientation. Variation of these fundamental characteristics influence the physical properties of the paper manufactured for printing, packaging, and other applications. Two of the three characteristics mentioned above, the fiber network structure and the basis weight uniformity, are affected by (a) the secondary flow structure of the jet before the impingement line, (b) amplification of secondary flow instabilities at the impingement line, and (c) the evolution of the layer along the forming section. For this reason, the headbox and the forming section are considered to be the most critical components in the paper making machine. With an increasing trend towards faster and more efficient paper machines and higher standards for the quality and the strength of the paper, a fundamental understanding of the wet-end dynamics, such as turbulence, flocculation, stock jet velocity, and impingement angle has become an important area of research (see §2).

In recent years, fine-scale velocity measurements, using the high speed digital imaging and LDV, in conjunction with numerical modeling, have considerably improved our understanding of the complex hydrodynamics of the headbox. To summarize, the turbulent flow from the headbox nozzle comprises complex stream-wise streaks in MD, a nonuniform profile in CD, and a large number of swirling eddies in ZD (which more or less form the cross sections of stream-wise streaks in MD). The distribution of stream-wise streaks in MD, usually, is quasi-periodic and is a manifestation of large-scale structures, superimposed on fine-scale turbulence. These complex patterns when combined with the free surface instabilities of the forming table produce wet streaks at the dry line. Larger and wider wet streaks degrade the homogeneity of the paper web resulting in a poor quality paper and cause variations in physical property ranging from 0.5 to 4.0 in. in CD. In stratified headboxes, the swirling motion in ZD may also cause mixing among the different layers and thus can jeopardize the grade of the paper (see §3).

The headbox geometry and dimension, along with the flow rate and fluid properties set the level of turbulence in the forming jet. The dimension, separation distance, and the

pattern or arrangement of the tubes in the tube bank along with the converging angle of the headbox and the slice lip determine the magnitude, dimension, and the dynamics of the small scale secondary flows and, consequently, the characteristics of stream-wise streaks in the free surface forming jet delivered at the slice (see §6).

The stream-wise streaks form in the forming jet, amplify upon impingement, and evolve along the forming wire with a characteristic growth and decay rate which determine the rate of growth and decay of a streak on the forming wire. Analysis of the streak formation and decay (§4) shows that these rate factors depend on the turbulence level of the flow, the average thickness of the layer, and the width (or wavelength) of SS. In general, the very narrow streaks grow and decay very rapidly. The growth rate of the wide streaks is relatively small. There exist a range of streaks with wave lengths in between, that grow to form wet streaks at the dry line.

The interaction and dynamics of the tube jets inside the headbox result in small scale CD oscillation or flapping of stream-wise streaks in the forming jet. This small scale CD motion results in small scale variations in fiber orientation and fiber network in the sheet. The most effective mechanism to eliminate this fundamental defect in paper forming is to control the small scale secondary flows induced by the tube jets. This can be achieved by modifications to the tubes in the tube bank.

Numerous experiments have been conducted on commercial headboxes (§7) using the high-speed digital imaging technique described in §6. Also experiments have been conducted on laboratory scale headboxes with and without guide sheets (§8). Current work is focussed on velocity profile measurements for individual tubes with the presence of fiber flocs that feed into the headbox.

# APPENDIX A

## Laser Doppler Velocimetry

An LDV system measures the velocity of suspended particles in the liquid, which pass through the interaction point of two laser beams. The backscattered light is interfered with a reference beam, and the Doppler signal from the LDV optical system is sent by optical fiber to a photodetector and converted to an electronic analog signal, resulting in a Doppler burst. The analog signal is connected to the digitizer input of a processor. Once the signal is digitized, the Doppler Signal Processor (DSP) board performs Doppler Fast Fourier Transform (DFFT) for each Doppler burst and calculates the Doppler frequency and the fluid velocity. Without frequency shift, the fringe pattern in the measurement probe is stationary. A particle crossing the beam generates a Doppler signal, $F_D$. With dual beam frequency shifting, one beam is shifted at a higher frequency, $F_H$, while the other beam is shifted at a lower frequency, $F_L$. This causes the optical fringes in the measurement probe to move in a direction from $F_H$ shifted beam to the $F_L$ shifted beam at a frequency equal to the difference of the two frequencies, $F_{shift}$, where $F_{shift} = F_H - F_L$. Thus, a particle passing through this probe and moving against the fringe generates a signal with an output frequency $F_{measured} = F_{shift} + F_D$. The particle's moving direction is defined as positive in the output of the processor. It means that positive direction in the flow field is defined as the direction of lower frequency–shifted beam toward higher frequency–shifted beam. The flow velocity $V_{real}$ is calculated by

$$V_{real} = F_D * D_s = (F_{measured} - F_{shift}) * D_s$$

where $D_s$ is the fringe separation distance.

# APPENDIX B

## Finding Jet's Velocity Profile Using Cross-Correlation of Digital Images

This method involves cross-correlation of subsequent high-speed digital images to determine the surface velocity profile of the forming jet. Use of cross-correlation methods to obtain velocity field is not a new practice. Cross-correlation flow meters [54-55] and Particle Image Velocimeters (PIV) are well established methods. The PIV, in particular, is a powerful method for velocity field measurements [56]. This method, however, is limited to transparent fluids with well-defined seeded particles. The fiber suspension in the headbox and the forming section are not transparent, and therefore, not accessible by PIV methods.

Here, we describe a simple method which has been used to measure the two-dimensional surface velocity profile of the forming jet. It takes advantage of the nonuniform patterns on the surface of the forming jet, recording the positions of the patterned structures using a high speed digital camera, and using cross-correlation techniques to produce a jet velocity profile.

In order to analyze the hydrodynamics of the forming table, a high-speed digital imaging system is used for high resolution imaging of the forming jet as it leaves the headbox. The individual grey scale images, or frames, taken 1 msec apart, are digital images of $384 \times 512$ pixels.

Camera orientation is very important to the success of this method. It is important that the camera be positioned normal to the forming table. If the images are from a different angle, velocity measurements would have to be adjusted and projected on the coordinate axes to account for the view angle. Furthermore, the camera must be angled so that the mean flow is in a north/south or east/west direction within the images produced. This will facilitate the line-by-line cross-correlation method described below. Samples of digital images are shown in previous publications [10].

These sample images show the type of data obtained by the digital camera. The camera picks up the detailed surface features of the forming jet. These features include turbulent patterns as well as mean flow streaks, crests, and troughs in the surface of the fluid. The

movement of these patterns during the 1 msec time lag between frames cross-correlated to estimate the forming jet surface velocity profile.

In order for this method to be most effective, the images must have a strong contrast with well-defined features. The original images may or may not have sharp contrast, depending on the lighting situation, the pattern of the forming jet, and other surrounding conditions. To account for this, contrast is enhanced using image analysis procedure [11]. Then two subsequent frames are compared to see how far the features of the image move during 0.001-sec interval between exposures. This program outputs a scalar value for the streamwise surface velocity component of the forming jet.

Figure B.1 shows two subsequent digital photographs of a section of a forming jet. Notice that the second image is very similar to the first, with the surface features shifted slightly to the left. The cross-correlation method takes advantage of this similarity by comparing the two images. It determines the distance that the features of the second image have been shifted relative to the first. This distance, the "lag" is then divided by the time elapsed between exposures to provide an estimate for the jet velocity profile.

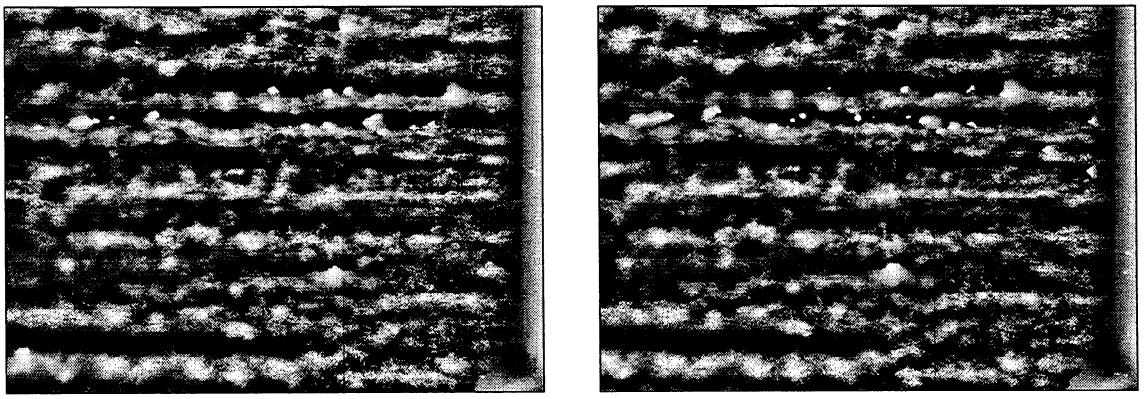

Figure B1: Digital images of the turbulent flow on the forming table, taken 1 msec apart. The MD is from right to left, and the photograph on the left is taken first. Notice the patterns due to turbulence superimposed on the mean streak patterns within the images. Each image represents a $4.7'' \times 6.3''$ region on the forming table

The features are compared via analysis of the gray scales, or light intensities of the digital images. The signals compared in this method are the gray scale values of bands of pixels aligned in the machine direction. Since this is the direction of the main flow, almost all of the motion occurring during the lag between the two frames occurs in this direction. Figure B.2 shows an example of these bands.

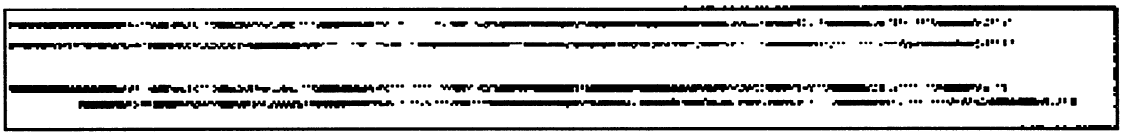

Figure B2: The top two lines are line segments from two digital images similar to those used in the cross-correlation program. At the bottom, the two images are lined up according to their respective gray scale values. The displacement of the bottom line is equal to the lag, or the distance, the line of fluid has moved within the 1-msec time interval between exposures

Gray scale intensities are converted to numerical values, and a FFT one-dimensional cross-correlation is carried out. If bands running the entire width of the image are used in the cross-correlation, an average jet velocity profile can be generated. This profile describes the jet velocity as a function of the location in the cross-machine direction. An average jet velocity profile generated for the case shown in Figures B.1 and B.2 is given in Figure B.3.

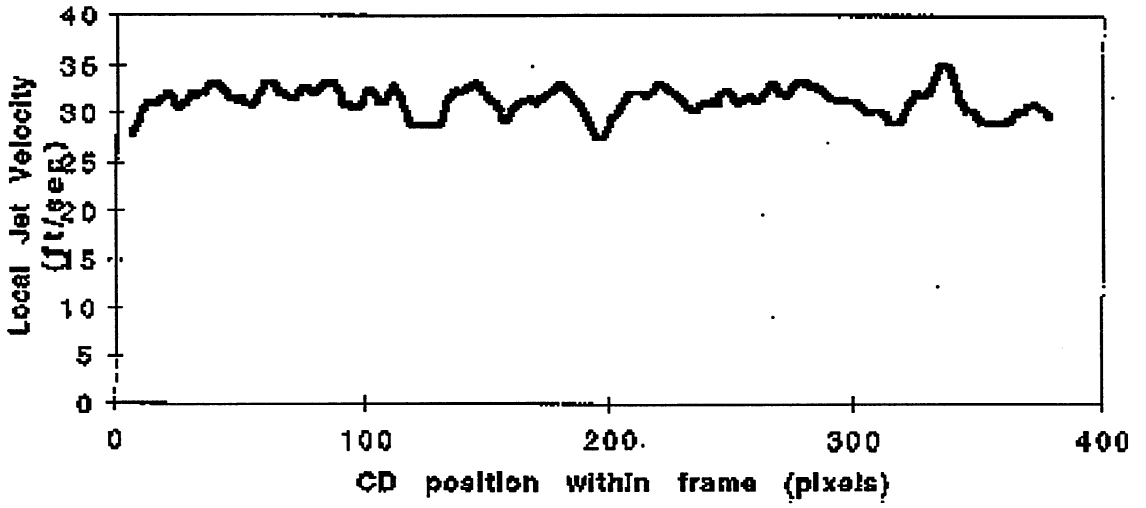


Figure B3: Average forming jet velocity profile determined by line-by-line cross-correlation

The trendline shown in Figure B.3 is a five-point moving average of the raw data produced by a cross-correlation routine. This graph shows the type of data that can be obtained via line-by-line cross-correlation of the entire image. One-dimensional cross-correlation can also be used to determine the local jet velocity at most points along the machine and cross-machine directions. This is done by choosing a different interrogation area. Instead of the entire bands used to determine the average velocity profile, subsets of these bands are used to determine local jet speeds.

To map the local jet speed profile of the forming jet, interrogation bands 64 pixels long, aligned along the mean flow direction, are defined. These interrogation bands are centered on each pixel of the image. Corresponding interrogation bands (bands centered at the same pixel location) from the two subsequent images are cross-correlated. The location of the correlation peak specifies the distance that the fluid surrounding the point has moved between exposures. As the time interval between the two images is known, the data can be used to calculate the local velocity of the forming jet.

The one-dimensional cross-correlation method, outlined above, does not provide the value of velocity for every point in the image. Since each interrogation band is 64 pixels long, and the local velocity at each pixel is determined by centering such a band at the pixel, velocity

values for areas to the extreme right and left of the image (with 32 pixels of the edge) are not available.

With the interrogation band length of only 64 pixels used in this method, small inconsistencies between the two images can cause relatively large errors. Even in the small time frame of 0.001 sec, many of the turbulent patterns within the digital frames may be distorted. For this reason, an estimate of the average jet velocity based on the total flow rate at the opening of the slice is used in the program, along with a set of user-defined tolerance values. The tolerance of the program is left to the discretion of the user. If the correlation peak is not within the allowed parameters, it is discarded.

# REFERENCES


1. Kenneth W. Britt (ed.), *Handbook of Pulp and Paper Technology*, Van Nostrand Reinhold Company, 1970.

2. J. Cox, Headboxes : New Technologies, New Challenges, *PIMA's PaperMaker*, March 1997.

3. G.A. Smook, *Handbook for Pulp & Paper Technologists*, TAPPI PRESS, Atlanta.

4. S.C. Pentaleo, *Modern Headboxes – Their Role and Capabilities in the Sheet Forming Process*, Lecture Notes.

5. B. Norman, Overview of the Physics of Forming, lecture notes.

6. K.L. Patrick, New Papermaking Technologies Pave Way to Higher Quality and Efficiency, *Pulp & Paper*, April 1998.

7. K.L. Patrick, New Papermaking Technologies Spur Competition in P & W Papermarkets, *Pulp & Paper*, May 1998.

8. K.L. Patrick, Paper Machine Developments Open Door to Higher Quality, Production Efficiency, *Pulp & Paper*, June 1998.

9. C.K. Aidun, Quantitative Evaluation of the Forming Jet Delivered from Four Different Hydraulic Headboxes Using High-Speed Digital Imaging, *Engineering & Papermakers Conference*, 1997, 1175–1195.

10. C.K. Aidun, Hydrodynamics of Streaks on the Forming Table, *Tappi Journal*, V.80(8), 1997.

11. C.K. Aidun and A.C. Ferrier, High-Speed Digital Imaging of Paper Forming: A Method for Quantitative Evaluation of Paper Forming Hydrodynamics, *Engineering & Papermakers Conference*, 1997, 883–887.

12. J. Zhu, Laser Doppler Velocimetry for Flow Measurements in Pulp and Paper Research, *TAPPI Engineering Conference*, 1996.

13. C.K. Aidun and A.E. Kovacs, Hydrodynamics of the Forming Section: the Origin of Nonuniform Fiber Orientation, *Tappi Journal*, V.78(11), 1997.

14. C.K. Aidun, Formation Hydrodynamics and Effects on Paper Physics, *International Paper Physics Conference*, 1995, 1–3.

15. M. Ullmar and B. Norman, Observation of Fiber Orientation in a Headbox Nozzle at Low Consistency, *Engineering & Papermakers Conference*, 1997, 865–873.

16. A.C. Li, E.B. Neill and T.D. Rogers, Jet Trajectory from a Converging Nozzle, *Engineering & Papermakers Conference*, 1997, 1197–1204.

17. M.S. Hall and T.G. Jackson, Small-Scale Variations in CD Strips Observed Using Ultrasonic Velocity Measurements, *Proceedings of International CD Symposium*, XIV IMEKO World Congress, Tampere, Finland, 1997, 174–179.

18. P.G. Drazin and W.H. Reid, *Hydrodynamics Instabilities*, Cambridge University Press, 1987, Cambridge, England.

19. C. Yih and A.C. Spengos, *TAPPI*, 42(5): 398(1959).

20. C. Yih and S.P. Lin, *TAPPI*, 47(2): 88(1964).

21. J. Shands, *J. Pulp Paper Sci.*, 17(3): J92(1991).

22. L.D. Soderberg and P.H. Alfredsson, *Engineering & Papermakers Conference*, 1997, 1205–1222.

23. I.L. Claeys, *Hydrodynamic Transport Properties of Suspensions of non- Brownian Prolate Spheroids*, Ph.D. Thesis, California Institute of Technology, 1991.

24. I.M. Hutten, *TAPPI 1994 Nonwovens Conference Proceedings*, TAPPI Press, Atlanta, p.241.

25. C.K. Aidun, N.G. Triantafillopoulos and J.D. Benson, *Phys. Fluid*, A.3, p.2081, 1991.

26. J.A. Liggett, *Fluid Mechanics*, 2nd edn., McGraw-Hill, New York, 1994, p.256.

27. A.O. Demuren and W. Rodi, *J. Fluid Mech.*, 140:189, 1984.

28. C.G. Speziale, *Ann. Rev. Fluid Mech.*, 23:107, 1991.

29. A. Huser and S. Biringer, *J. Fluid Mech.*, 257:65, 1993.

30. S. Gavrilakis, *J.Fluid Mech.*, 244:101, 1992.

31. B.F. Gessner and J.B. Jones, *J.Fluid Mech.*, 23:689, 1965.

32. A. Melling and J.H. Whitelaw, *J. Fluid Mech.*, 78:289, 1976.

33. T. Wei and W.W. Willmarth, *J. Fluid Mech.*, 204:57, 1989.

34. C.G. Speziale, *J. Fluid Mech.*, 178:459, 1987.

35. K. Hanzalic and B.E. Launder, *J. Fluid Mech.*, 52:609, 1972.

36. M. Colombini, *J. Fluid Mech.*, 254:701, 1993.

37. I. Nezu, H. Nakagawa and A. Tominaga, *Turbulent Shear Flows IV*, Springer Verlag, New York, 1985, pp.246–260.

38. D. Naot and W. Rodi, *ASCE* 108(HY8): 948, 1982.

39. J.O. Hinze, *Turbulence*, McGraw-Hill, New-York, 1975.

40. J.F. McKibben and C.K. Aidun, *J. Comput. Phys.*, in press.

41. J.F. McKibben and C.K. Aidun, *Tappi J.*, 77(5):143, 1994,in press.

42. J. Kim and P. Moin, *J. Comput. Phys.*, 59:308, 1984.

43. A. Huser and S. Biringer, *Int. J. Num. Methods in Fluids*, 14:1087, 1992.

44. M.S. Engelman, *FIDAP: Fluid Dynamics Analysis Package*, Fluid Dynamics International, Evanston, 1992.

45. C.G. Speziale, *Transactions of the ASME*, 108:118, 1986.

46. H.J. Perkins, *J. Fluid Mech.*, 44:721, 1970.

47. C.K. Aidun, A Fundamental Opportunity to Improve Paper Forming, *Tappi J.*, 79(6), 55, 1996.

48. H. Hauptmann, R. Vyse and J. Mardon, The Wake Effects as Applied to Modern Hydraulic Headboxes, Part I and II, *Pulp and Paper Canada*, 91(9 and 10), T357 and T369, 1990.

49. P.E. Wrist, Dynamics of Sheet Formation in the Fourdrinier Machine, in *Formation of Structure of Paper - 2, Trans. Symp.*, held at Oxford, London, Sept. 1961 (F. Bolam ed.), Tech. Ser. Brit. Paper and Board Makers Assoc., 839, 1962.

50. L. Lindquist, Structure of the Flow from Paper Machine Headboxes: A Model Study, Licentiate Thesis, Lulea University of Technology, Sweden.

51. Bloomfield, *Fourier Analysis of Time Series: An Introduction*, 1976, John Wiley & Sons, Inc.

52. W.H. Press, S.A. Teukolsky, W.T. Vetterling and B.P. Flannery, *Numerical Recipes in C*, Second Edition(ch. 12 & 13), Cambridge University Press, 1992.

53. C.K. Aidun, P.J. McKay, and X.L. Ye, *Fundamentals of Headbox and Forming Hydrodynamics*, Status Report for Project F005, IPST, 1998.

54. C.K. Aidun, X.L. Ye, and P.J. McKay, *Headbox and Forming Hydrodynamics*, Status Report for Project F005, IPST, 1997.

55. M.S. Beck, Correlation in Instruments: Cross-Correlation Flowmeters, *J. Phys. E. Sci. Instrum.*, 14, 1981, pp. 7–19.

56. F. Frigerio and D.P. Hart, Velocity Field Measurements of a Confined Swirling Flow Using Digital Particle Image Velocimetry Cinematography, *1997 ASME Fluids Engineering Division Summer Meeting*, June 1997.